Available online at www.sciencedirect.com
ScienceDirect
International Journal of Heat and Fluid Flow 29 (2008) 504–526
International Journal of HEAT AND FLUID FLOW
www.elsevier.com/locate/ijhff

Predicting transition in two- and three-dimensional separated flows

L. Cutrone [a], P. De Palma [b], G. Pascazio [b,*], M. Napolitano [b]

[a] Centro Italiano Ricerche Aerospaziali, CIRA, Via Maiorise, 81043 Capua (CE), Italy
[b] Dipartimento di Ingegneria Meccanica e Gestionale, DIMeG, Centro di Eccellenza in Meccanica Computazionale, CEMeC, Politecnico di Bari, Via Re David 200, 70125 Bari, Italy

Received 6 June 2007; received in revised form 21 November 2007; accepted 26 November 2007
Available online 10 January 2008

Abstract

This paper is concerned with the numerical prediction of two- and three-dimensional transitional separated flows of turbomachinery interest. The recently proposed single-point transition model based on the use of a laminar kinetic energy transport equation is considered, insofar as it does not require to evaluate any integral parameter, such as boundary-layer thickness, and is thus directly applicable to three-dimensional flows. A well established model, combining a transition-onset correlation with an intermittency transport equation, is also used for comparison. Both models are implemented within a Reynolds-averaged Navier–Stokes solver employing a low-Reynolds-number k–ω turbulence model. The performance of the transition models have been evaluated and tested versus well-documented incompressible flows past a flat plate with semi-circular leading edge, namely: tests T3L2, T3L3, T3L5, and T3LA1 of ERCOFTAC, with different Reynolds numbers and free-stream conditions, the last one being characterized by a non-zero pressure gradient. In all computations, the first model has proven as adequate as or superior to the second one and has been then applied with success to two more complex test cases, for which detailed experimental data are available in the literature, namely: the two- and three-dimensional flows through the T106 linear turbine cascade.

Keywords: RANS equations; Transition models; Intermittency factor; Laminar kinetic energy; Finite volume method

1. Introduction

Laminar-turbulent transition plays a crucial role in many flows of engineering interest; in particular, the flow through a low-pressure turbine or a compressor is highly influenced by transition, which has a remarkable impact on losses and heat transfer. Therefore, modeling transition correctly is essential to improve the performance of modern turbomachinery, and is a very challenging task for state-of-the-art CFD codes, transition being a highly non-linear phenomenon which involves a wide range of scales.

In general, depending on the pressure gradient and the free-stream turbulence intensity, three main transition mechanisms can be observed (Mayle, 1991). The first one (*natural* transition) begins with a weak instability in the laminar boundary-layer and then progresses by the amplification of Tollmien–Schlichting waves; the second one, commonly encountered in turbomachinery flows, bypasses the previous instability mechanism due to the large disturbances in the outer flow region (*bypass* transition); the third one is referred to as *separated-flow* transition, insofar as it occurs within a separated boundary layer, and may or may not experience a natural growth mechanism.

The basic mechanism of boundary-layer transition under different flow conditions can be studied using direct numerical simulations and large eddy simulations for moderate values of the Reynolds number (Re). However, due to their high computational costs, such techniques are not applicable to high-Re complex turbomachinery flows. In such cases, numerical models based on the solution of the Reynolds-averaged Navier–Stokes (RANS) equations are

* Corresponding author. Tel.: +39 080 5963221; fax: +39 080 5963411.
E-mail addresses: l.cutrone@cira.it (L. Cutrone), depalma@poliba.it (P. De Palma), pascazio@poliba.it (G. Pascazio), napolita@poliba.it (M. Napolitano).

0142-727X/$ - see front matter © 2007 Elsevier Inc. All rights reserved.
doi:10.1016/j.ijheatfluidflow.2007.11.005

Nomenclature

c	chord
C_f	skin friction coefficient, $\tau_w/(1/2u_\infty^2\rho_\infty)$
D	dissipation term, source term
f	damping function
H	specific total enthalpy
K	acceleration parameter, $(\nu/u^2)(du/dx)$
k	turbulence kinetic energy
n	spot generation rate
$\hat{n}$	nondimensional spot generation rate
P	production term
p	pressure
p_t	total pressure
Re_θ	momentum thickness Reynolds number, $(\theta u_\infty)/\nu$
S	source term, magnitude of mean strain-rate-tensor, $\sqrt{2S_{ij}S_{ij}}$
S_{ij}	strain-rate-tensor components
s	pitch
t	time
Tu	turbulence intensity, $100\sqrt{2k/3u_\infty^2}$
U	specific total internal energy
u	velocity magnitude
u_i, u_j	velocity components
u_∞	local free-stream velocity
u_{in}	inlet velocity
x	curvilinear coordinate
y^+	$(y_n u_\tau)/\nu$
y_n	normal distance to wall
γ	intermittency factor
δ	boundary-layer thickness
δ_{ij}	Kroneker delta
ε	turbulence dissipation rate
θ	momentum thickness
λ	length scale
λ_T	turbulence length scale
μ	molecular viscosity
μ_T	eddy viscosity
ν	μ/ρ
ν_T	μ_T/ρ
ρ	density
σ	Emmons spot propagation parameter
τ_{ij}	stress-tensor components
ω	specific dissipation rate, loss coefficient, $(p_{t1}-p_t)/(p_{t1}-p_2)$
Ω	magnitude of mean rotation tensor, $\sqrt{2\Omega_{ij}\Omega_{ij}}$
Ω_{ij}	mean rotation tensor components

Subscripts

ax	axial
in	inlet
is	isentropic
L	laminar
l	large scale
le	leading-edge
s	small scale
T	turbulent
t	onset of transition
∞	free-stream

still warranted. On the other hand, in spite of the efforts of several researchers aimed at developing low-Reynolds-number turbulence models with some built-in transition modeling capability, i.e., models based on either non-linear eddy viscosity methods (Craft et al., 1997; Chen et al., 1998) or Reynolds-stress transport equations (Hanialić et al., 1997), to-date RANS methods have been proven inadequate for predicting the transition under general flow conditions (Savill, 2002; Westin and Henkes, 1997; De Palma, 2002; De Palma, 2006).

It is then clear that a more specific transition model has to be developed and implemented, e.g., a model based on the intermittency factor, which represents the fraction of time the flow is turbulent (Mayle, 1991). Several methods have been proposed to compute such an intermittency factor, which are based on empirical algebraic correlations (Mayle, 1991; Michelassi et al., 1999) or on the solution of an additional transport equation (Cho and Chung, 1992; Suzen and Huang, 2000; Steelant and Dick, 1996; Vicedo et al., 2004). One disadvantage of these intermittency-type models is that they rely on empirical correlations based on non-local parameters for the transition-onset prediction, such as boundary-layer displacement or momentum thickness, which are strictly two-dimensional concepts, and thus are difficult to evaluate in complex geometries. A further difficulty is encountered in transitional flows with a separation bubble, when transition may occur either in the attached- or separated-flow region; e.g., in the case of the interaction of an unsteady upstream wake with the boundary-layer in high-lift low-pressure turbine cascades (Hodson and Howell, 2005), where intermittency transport models need two different transition-onset criteria (Lodefier and Dick, 2005; Suzen and Huang, 2005). Finally, even if the intermittency factor is well modeled, computing transitional flows by multiplying it times the eddy viscosity coefficient could still produce considerable errors in the calculations of the shear stresses (Mayle, 1991).

Therefore, a more general method, that can be applied to a wide range of flow conditions as well as to three-dimensional geometries, is needed to improve the design of advanced turbomachinery. In this context, pre-transitional boundary-layer fluctuations, induced by the free-

stream turbulence in bypass transitional flows, are recognized to play a fundamental role in the definition of adequate models (Mayle and Schulz, 1997; Volino, 2005; Lardeau et al., 2007; Praisner and Clark, 2007). In particular, following the approach proposed by Mayle and Schulz (1997) to compute the turbulence kinetic energy in the transitional region, Lardeau et al. (2004) and Lardeau and Leschziner (2006) proposed a means to combine the low-Reynolds-number explicit algebraic Reynolds-stress model of Abe et al. (2003) with an intermittency-type approach using a transport equation for the laminar kinetic energy equation. However, such a model, which again employs an algebraic correlation for evaluating the intermittency factor and a second correlation for detecting the transition onset, still suffers from the aforementioned intermittency-approach drawbacks. Therefore, Walters and Leylek (2004) provided a single-point transition model, independent of the intermittency factor: following Mayle and Schulz (1997), they model the pre-transitional stream-wise boundary-layer fluctuations induced by the free-stream turbulence by introducing an additional transport equation for the laminar kinetic energy, which determines the transition-onset and/or length without any need for nonlocal parameters.

Given the state-of-the-art described above, it seems useful and worthwhile to evaluate the performance of transition models versus well-documented flows, with particular attention to turbomachinery applications. In a recent paper, Cutrone et al. (2007) have combined six state-of-the-art transition models with the low-Reynolds-number $k-\omega$ turbulence model (Wilcox, 1998), to compute three incompressible flows past flat plates as well as a two-dimensional flow past a turbine cascade, all without separation. Five models combine a transition-onset correlation with an intermittency factor prediction, the sixth one being the novel single-point model of Walters and Leylek (2004). Although none of the models was found fully satisfactory, the last one was capable of simulating two-dimensional attached bypass transitional flows as well as, or even better than, the most satisfactory among the others, namely the Suzen and Huang (2000) model.

In this work, the code developed by Cutrone et al. (2007) is used at first to evaluate the two aforementioned models versus well-documented two-dimensional separated flows past a flat plate with semi-circular leading edge, namely, tests T3L2, T3L3, T3L5, and T3LA1 of ERCOFTAC, with different Reynolds numbers and free-stream conditions, the last one being characterized by a non-zero pressure gradient. The model of Walters and Leylek (2004) again performed as well as, or even better than, that of Suzen and Huang (2000), resulting the most suitable model for predicting turbomachinery-flow transition; therefore, it has been applied to compute the two-dimensional flow through the T106 linear turbine cascade. Finally, the code of Cutrone et al. (2007) has been extended to three-dimensional flows and applied to evaluate the Walters and Leylek (2004) transition model versus the complex three-dimensional flow through the same T106 linear turbine cascade, for which detailed experimental data are available in the literature.

After a brief description of the governing equations, the two transition models are described in detail, whereas the numerical method is only outlined. The test problems are then described together with the numerical results. Finally, some brief conclusions are drawn.

2. Reynolds-averaged Navier–Stokes equations

The Reynolds-averaged Navier–Stokes (RANS) equations are written in terms of Favre mass-averaged variables and coupled with the low-Reynolds-number $k-\omega$ turbulence model

$$\frac{\partial \rho}{\partial t}+\frac{\partial}{\partial x_j}(\rho u_j)=0, \tag{1}$$

$$\frac{\partial(\rho u_i)}{\partial t}+\frac{\partial}{\partial x_j}(\rho u_j u_i)=-\frac{\partial p}{\partial x_i}+\frac{\partial \hat{\tau}_{ij}}{\partial x_j}, \tag{2}$$

$$\frac{\partial(\rho U)}{\partial t}+\frac{\partial}{\partial x_j}(\rho u_j H) = \frac{\partial}{\partial x_j}\left[u_i\hat{\tau}_{ij}+(\mu+\sigma^*\mu_{\mathrm{T}})\frac{\partial k}{\partial x_j}-q_j\right], \tag{3}$$

$$\frac{\partial(\rho k)}{\partial t}+\frac{\partial}{\partial x_j}(\rho u_j k)=\tau_{ij}\frac{\partial u_i}{\partial x_j}-\beta^*\rho\omega k + \frac{\partial}{\partial x_j}\left[(\mu+\sigma^*\mu_{\mathrm{T}})\frac{\partial k}{\partial x_j}\right], \tag{4}$$

$$\frac{\partial(\rho\omega)}{\partial t}+\frac{\partial}{\partial x_j}(\rho u_j \omega)=\frac{\alpha\omega}{k}\tau_{ij}\frac{\partial u_i}{\partial x_j}-\beta\rho\omega^2 + \frac{\partial}{\partial x_j}\left[(\mu+\sigma\mu_{\mathrm{T}})\frac{\partial \omega}{\partial x_j}\right]. \tag{5}$$

U and H are the specific total energy and enthalpy comprehensive of the turbulence kinetic energy, k; the eddy viscosity, μ_{T}, is defined in terms of k and of the specific dissipation rate, ω, according to the $k-\omega$ turbulence model of Wilcox (1998),

$$\mu_{\mathrm{T}}=\alpha^*\frac{\rho k}{\omega}, \tag{6}$$

and ω is limited by the *realizability* constraint of Durbin (1996)

$$\omega=\max\left(\omega,\frac{1}{(1/0.09)\sqrt{3/(8S^2)}}\right).$$

Moreover, $\hat{\tau}_{ij}$ indicate the sum of the molecular and Reynolds (τ_{ij}) stress-tensor components. According to the Boussinesq approximation, one has

$$\hat{\tau}_{ij}=(\mu+\mu_{\mathrm{T}})\left[\frac{\partial u_i}{\partial x_j}+\frac{\partial u_j}{\partial x_i}-\frac{2}{3}\frac{\partial u_k}{\partial x_k}\delta_{ij}\right]-\frac{2}{3}\rho k\delta_{ij}. \tag{7}$$

Finally, the heat flux vector components, q_j, are given as

$$q_j = -\left(\frac{\mu}{Pr} + \frac{\mu_T}{Pr_T}\right)\frac{\partial h}{\partial x_j}, \tag{8}$$

where $Pr = 0.71$ and $Pr_T = 0.9$ are the laminar and turbulent Prandtl numbers, respectively. Sutherland's law is used to compute the molecular viscosity coefficient and the closure coefficients of the low-Reynolds-number $k-\omega$ model are given as (Wilcox, 1998)

$$\alpha^* = \frac{\alpha_0^* + Re_T/R_k}{1 + Re_T/R_k}, \quad \alpha = \frac{5}{9\alpha^*}\frac{\alpha_0 + Re_T/R_\omega}{1 + Re_T/R_\omega}, \quad Re_T = \frac{\rho k}{\omega\mu},$$

$$\beta^* = \frac{9}{100}\frac{5/18 + (Re_T/R_\beta)^4}{1 + (Re_T/R_\beta)^4}, \quad \beta = \frac{3}{40}, \quad \sigma^* = \sigma = \frac{1}{2},$$

$$\alpha_0^* = \frac{\beta}{3}, \quad \alpha_0 = \frac{1}{10}, \quad R_\beta = 8, \quad R_k = 6, \quad R_\omega = 2.7.$$

3. Laminar-turbulent transition

This section provides a detailed description of: (i) the main transition model employed in the present work (Walters and Leylek, 2004), which does not rely on the intermittency factor concept but is a single-point transition model based on a transport equation for the laminar kinetic energy; (ii) the Suzen and Huang (2000) model, combining a correlation for predicting the transition onset with an intermittency transport model, which is used for comparison.

3.1. The Walters and Leylek model

This model was originally proposed by Walters and Leylek (2004, 2005) and has been proven effective in computing two-dimensional attached bypass transitional flows (Cutrone et al., 2007). The model, called here M1, is based on an eddy viscosity coefficient, determined by using three transport equations for the turbulence kinetic energy, k, the laminar kinetic energy, k_L, and the specific dissipation rate, ω, respectively

$$\frac{\partial(\rho k)}{\partial t} + \frac{\partial}{\partial x_j}(\rho u_j k) = \rho P_k + \rho R - \rho\varepsilon - \rho D_T + \frac{\partial}{\partial x_j}\left[\left(\mu + \frac{\rho\alpha_T}{\sigma_k}\right)\frac{\partial k}{\partial x_j}\right], \tag{9}$$

$$\frac{\partial(\rho k_L)}{\partial t} + \frac{\partial}{\partial x_j}(\rho u_j k_L) = \rho P_{k_L} - \rho R - \rho D_L + \frac{\partial}{\partial x_j}\left[\mu\frac{\partial k_L}{\partial x_j}\right], \tag{10}$$

$$\frac{\partial(\rho\omega)}{\partial t} + \frac{\partial}{\partial x_j}(\rho u_j \omega) = \rho P_\omega + \rho C_{\omega R}\frac{\omega}{k}R - \rho C_{\omega 2}\omega^2 + \rho C_{\omega 2} f_\omega \alpha_T \left(\frac{\lambda_{eff}}{\lambda_T}\right)^{4/3}\frac{\sqrt{k}}{y_n^3} + \frac{\partial}{\partial x_j}\left[\left(\mu + \frac{\rho\alpha_T}{\sigma_\omega}\right)\frac{\partial\omega}{\partial x_j}\right]. \tag{11}$$

Eqs. (9)–(11) substitute the equations of the original turbulence model, namely, Eqs. (4) and (5), respectively. The laminar kinetic energy is associated with the *non-turbulent* stream-wise fluctuations in the pre-transitional boundary layer, defined in the work of Mayle and Schulz (1997). The effective length scale, λ_{eff}, is the minimum length scale of the fluctuations contributing to the production of these non-turbulent perturbations by means of the splat mechanism described by Walters and Leylek (2005) and Volino (1998). It is estimated as

$$\lambda_{eff} = \min(C_\lambda y_n, \lambda_T), \tag{12}$$

where $C_\lambda = 2.495$, $\lambda_T = k^{3/2}/\varepsilon$ is the turbulence length scale, $\varepsilon = \omega k$ is the turbulence dissipation rate, and y_n is the distance from the nearest wall. The turbulence kinetic energy can be divided into small-scale energy, $k_{T,s}$, and large-scale energy, $k_{T,l}$, as follows:

$$k_{T,s} = k(\lambda_{eff}/\lambda_T)^{2/3}, \quad k_{T,l} = k\left[1 - (\lambda_{eff}/\lambda_T)^{2/3}\right]; \tag{13}$$

the former interacts with the mean-flow as a typical turbulence energy, whereas the latter only contributes to the production of k_L.

The first term in the right-hand side of Eq. (9) is the turbulence production due to turbulent fluctuations

$$P_k = \nu_{T,s}\left(\frac{\partial u_i}{\partial x_j} + \frac{\partial u_j}{\partial x_i} - \frac{2}{3}\frac{\partial u_k}{\partial x_k}\delta_{ij}\right)\frac{\partial u_i}{\partial x_j} - \frac{2}{3}k_{T,s}\frac{\partial u_k}{\partial x_k}, \tag{14}$$

where the small-scale viscosity, $\nu_{T,s}$, is defined as

$$\nu_{T,s} = \min\left(f_\mu f_{INT} C_\mu \sqrt{k_{T,s}}\lambda_{eff}, \frac{2.5\varepsilon_{TOT}}{S^2}\right). \tag{15}$$

In the equation above, C_μ is the turbulent viscosity coefficient, taken to be 0.09 in fully turbulent regions, and f_μ and f_{INT} are damping functions used to impose near-wall viscous effects and to prevent the overprediction of momentum near completion of the bypass transition, respectively. The functional forms of these coefficients are given as (Walters and Leylek, 2004, 2005)

$$f_\mu = 1 - \exp\left(-\frac{\sqrt{Re_{T,s}}}{A_\mu}\right), \quad Re_{T,s} = \frac{k_{T,s}^2}{\nu\varepsilon}, \quad A_\mu = 6.75;$$

$$f_{INT} = \min\left(\frac{k}{C_{INT}k_{TOT}}, 1\right), \quad C_{INT} = 0.75.$$

In Eqs. (9) and (11), the turbulence scalar diffusivity is defined as

$$\alpha_T = f_\mu C_\mu \sqrt{k}\lambda_{eff}, \tag{16}$$

and

$$\sigma_k = 1, \quad \sigma_\omega = 1.17.$$

The first term in the right-hand side of Eq. (10) is the production of the laminar kinetic energy due to large-scale turbulent fluctuations,

$$P_{k_L} = \nu_{T,l}\left(\frac{\partial u_i}{\partial x_j} + \frac{\partial u_j}{\partial x_i} - \frac{2}{3}\frac{\partial u_k}{\partial x_k}\delta_{ij}\right)\frac{\partial u_i}{\partial x_j} - \frac{2}{3}k_{T,l}\frac{\partial u_k}{\partial x_k}. \tag{17}$$

The large-scale viscosity, $\nu_{T,l}$, is defined as

$$\nu_{T,l} = \min\left[f_{\tau,l}C_{l1}\left(\frac{\Omega\lambda_{eff}^2}{\nu}\right)\sqrt{k_{T,l}}\lambda_{eff}, \frac{0.5k_{T,l}}{S}\right], \quad (18)$$

where $f_{\tau,l}$ is a time-scale-based damping function (Walters and Leylek, 2004)

$$f_{\tau,l} = 1 - \exp\left[-C_{\tau,l}\left(\frac{\tau_m}{\tau_{T,l}}\right)^2\right]$$

with

$$\tau_m = \frac{1}{\Omega}, \quad \tau_{T,l} = \frac{\lambda_{eff}}{\sqrt{k_{T,l}}}, \quad C_{l1} = 3.4\times10^{-6}, \quad C_{\tau,l} = 4360.$$

The term R in Eqs. (9)–(11) represents the effect of the stream-wise fluctuations on turbulence during bypass transition,

$$R = C_R\beta_{BP}k_L\omega\left(\frac{\lambda_T}{\lambda_{eff}}\right), \quad (19)$$

where β_{BP} is a threshold function defined as

$$\beta_{BP} = 1 - \exp\left(-\frac{\phi_{BP}}{A_{BP}}\right),$$

$$\phi_{BP} = \max\left[\left(\frac{\sqrt{k}y_n}{\nu} - C_{BP,crit}\right), 0\right], \quad (20)$$

and the closing coefficients read

$$C_R = 0.05, \quad A_{BP} = 3, \quad C_{BP,crit} = 12.$$

The terms D_T and D_L in Eqs. (9) and (10) are the turbulent and laminar near-wall dissipation terms, respectively, given as (Walters and Leylek, 2004)

$$D_T = 2\nu\frac{\partial\sqrt{k}}{\partial x_j}\frac{\partial\sqrt{k}}{\partial x_j}, \quad D_L = 2\nu\frac{\partial\sqrt{k_L}}{\partial x_j}\frac{\partial\sqrt{k_L}}{\partial x_j}. \quad (21)$$

According to these definitions, the total dissipation rate of the fluctuation energy, ε_{TOT}, is defined as the sum of the dissipation rate of turbulence, ε, and of the near-wall dissipation terms, D_T and D_L.

The production term P_ω in Eq. (11) takes the form

$$P_\omega = \frac{\omega}{k}C_{\omega1}\left[\nu_{T,\omega}\left(\frac{\partial u_i}{\partial x_j} + \frac{\partial u_j}{\partial x_i} - \frac{2}{3}\frac{\partial u_k}{\partial x_k}\delta_{ij}\right)\frac{\partial u_i}{\partial x_j} - \frac{2}{3}k_{T,s}\frac{\partial u_k}{\partial x_k}\right], \quad (22)$$

where $C_{\omega1} = 0.44$ and

$$\nu_{T,\omega} = f_\mu f_{INT}C_\mu\sqrt{k_{T,s}}\lambda_{eff}$$

corresponds to the small-scale unlimited viscosity in Eq. (15). The coefficients $C_{\omega R}$ and $C_{\omega2}$ in Eq. (11) are computed as

$$C_{\omega R} = 1.5\left(\frac{\lambda_T}{\lambda_{eff}}\right)^{2/3} - 1 \quad \text{and} \quad C_{\omega2} = 0.92\left(\frac{\lambda_{eff}}{\lambda_T}\right)^{4/3}. \quad (23)$$

The influence of turbulent and laminar fluctuations on the mean-flow and energy equations is accounted for by defining a total eddy viscosity which is used to model the Reynolds-stress tensor as

$$-\rho\overline{u_iu_j} = \nu_{TOT}\left(\frac{\partial u_i}{\partial x_j} + \frac{\partial u_j}{\partial x_i} - \frac{2}{3}\frac{\partial u_k}{\partial x_k}\delta_{ij}\right) - \frac{2}{3}\rho k_{TOT}\delta_{ij}, \quad (24)$$

where $\nu_{TOT} = \nu_{T,s} + \nu_{T,l}$ and $k_{TOT} = k + k_L = k_{T,s} + k_{T,l} + k_L$.

3.2. The Suzen and Huang model

This model, called here M2, combines a transition-onset correlation with an intermittency transport model so as to replace the eddy viscosity coefficient μ_T in Eqs. (3)–(8) with the product $\gamma\mu_T$, γ being the intermittency factor.

Two transition-onset correlations are employed, being suitable for attached- and separated-flow transition, respectively: the onset is triggered when either condition is satisfied.

The transition-onset for attached flow has been proposed by Suzen et al. (2002) for evaluating the transition-onset point on the basis of the corresponding value of the Reynolds number based on the boundary-layer momentum thickness, Re_{θ_t}

$$Re_{\theta_t} = (120 + 150\mathrm{Tu}_{le}^{-2/3})\coth[4(0.3 - |K_{min}|\times10^5)]. \quad (25)$$

In the equation above, K_{min} indicates the smallest value of the pressure gradient parameter $K_\infty = (\nu_\infty/u_\infty^2)(\mathrm{d}u_\infty/\mathrm{d}x)$ in the deceleration region, evaluated at the local edge of the boundary-layer. According to the correlations provided by Mayle (1991), the maximum value for $|K_{min}|$ is 3×10^{-6}.

The base mechanism of the separated-flow transition has been described in detail by Mayle (1991), see Fig. 1, which provides a sketch of the time-averaged transition region. After flow separation, there is a low-pressure gradient region (upstream region) followed by a pressure recovery (downstream region). The upstream region is composed of a laminar shear flow, between the abscissae x_s (separation) and x_t (transition-onset), and a transition region between the abscissae x_t and x_T (end of transition). In the downstream region, the flow is turbulent and reattaches

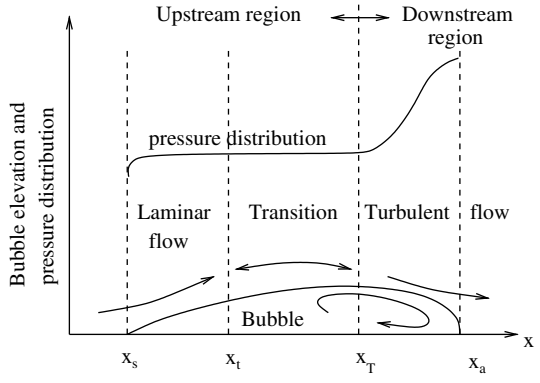

Fig. 1. Schematic of separated-flow transition.

at x_r. Separation bubble experiments have also shown that decreasing the free-stream turbulence level increases the size of the separation bubble and delays transition (Malkiel and Mayle, 1996).

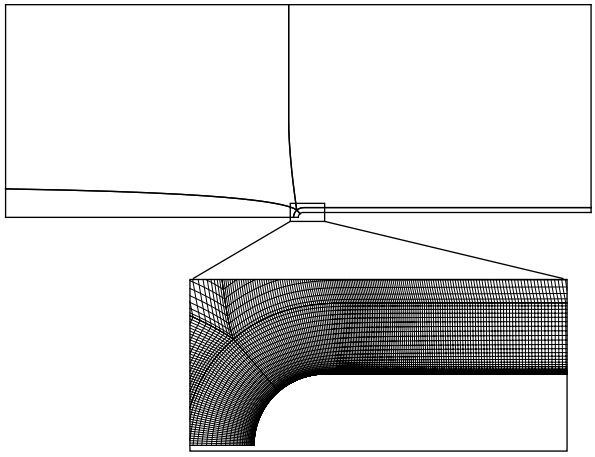

Fig. 2. T3L test case: computational domain and partial view of the grid at the leading-edge region.

Table 1
T3L test cases: flow conditions at 6 mm

Case	u_∞ (m/s)	Re	Tu_∞ (%)
T3L2	5	3293	0.632
T3L3	5	3293	2.31
T3L5	2.5	1647	2.30

Table 2
T3L test cases: inlet boundary conditions

Case	u_{in} (m/s)	Tu_{in} (%)	$\lambda_{T,in}$ (mm)	$\lambda_{T,n}$ (mm)	$\lambda_{T,exp}$ (mm)
T3L2	4.798	1.08	2.54	4.00	4.72
T3L3	4.798	3.90	8.91	13.7	13.91
T3L5	2.387	3.90	8.77	13.5	13.0

Here, the transition-onset in separated flows is evaluated by means of the correlation proposed by Mayle (1991) using different set of experimental data

$$(Re_x)_{st} = 1000 Re_{\theta_s}^{0.7}, \tag{26}$$

where

$$(Re_x)_{st} = \frac{u_s(x_t - x_s)}{\nu_s}, \quad Re_{\theta_s} = \frac{u_s \theta_s}{\nu_s}, \tag{27}$$

u_s, θ_s, and ν_s being the free-stream velocity, the momentum thickness and the kinematic viscosity at the separation point. Provided that such values are known, Eqs. (26) and (27) allow one to evaluate the distance between the transition-onset point and the separation one, $x_t - x_s$.

The intermittency transport model used here is that proposed by Suzen and Huang (2000): it combines the intermittency factor transport equation models of Steelant and Dick (1996), based on the correlation of Dhawan and Narasimha (1958) and Cho and Chung (1992), using a blending function to predict both the experimentally observed stream-wise intermittency variations and the correct behaviour in the cross-stream direction. The transport equation for the intermittency factor, γ, reads

$$\frac{\partial(\rho\gamma)}{\partial t} + \frac{\partial(\rho u_j \gamma)}{\partial x_j} = D_\gamma + S_\gamma, \tag{28}$$

where D_γ is the diffusion term, namely,

$$D_\gamma = \frac{\partial}{\partial x_j}\left\{ \left[(1-\gamma)\gamma\sigma_{\gamma_l}\mu + (1-\gamma)\sigma_{\gamma_t}\mu_T\right] \frac{\partial \gamma}{\partial x_j} \right\} \tag{29}$$

and

$$S_\gamma = (1-\gamma)[(1-F)T_0 + F(T_1 - T_2)] + T_3, \tag{30}$$

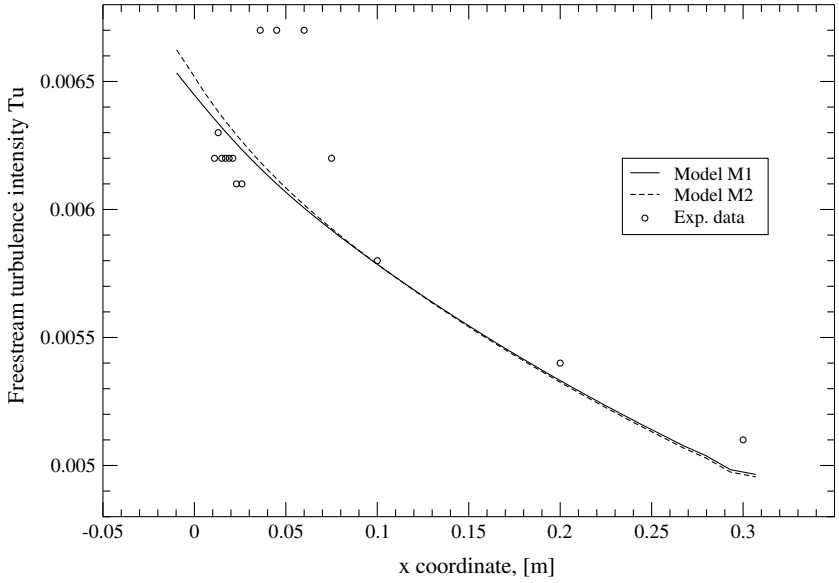

Fig. 3. T3L2 test case: free-stream turbulence intensity decay.

where F is the blending function. The first term, T_0, derives from the model of Steelant and Dick (1996),

$$T_0 = C_0 \rho \sqrt{u_k u_k}\beta(x), \tag{31}$$

where $\beta(x) = 2f(x)f'(x)$ and the function $f(x)$ is the following polynomial interpolation function for $\hat{n}\sigma(Re_x - Re_{x_t})^2$ around the transition-onset point, x_t (Steelant and Dick, 1996)

$$f(x) = \frac{ax'^4 + bx'^3 + cx'^2 + dx' + e}{h_1 x' + h_2}, \tag{32}$$

with $x' = x - x_t$, and

$$a = 50\sqrt{\frac{n\sigma}{u}}, \quad b = -0.4906, \quad c = 0.204\left(\frac{n\sigma}{u}\right)^{-0.5},$$
$$d = 0, \quad e = 0.04444\left(\frac{n\sigma}{u}\right)^{-1.5}, \quad h_1 = 50, \quad h_2 = 10e. \tag{33}$$

Eq. (31) is based on the following correlation of Dhawan and Narasimha (1958) for the intermittency distribution along the flow direction

$$\gamma = 1 - \exp[-\hat{n}\sigma(Re_x - Re_{x_t})^2], \tag{34}$$

where x is the curvilinear coordinate along the wall, $Re_x = u_\infty x/v_\infty$, $\hat{n} = nv_\infty^2/u_\infty^3$ is the nondimensional production

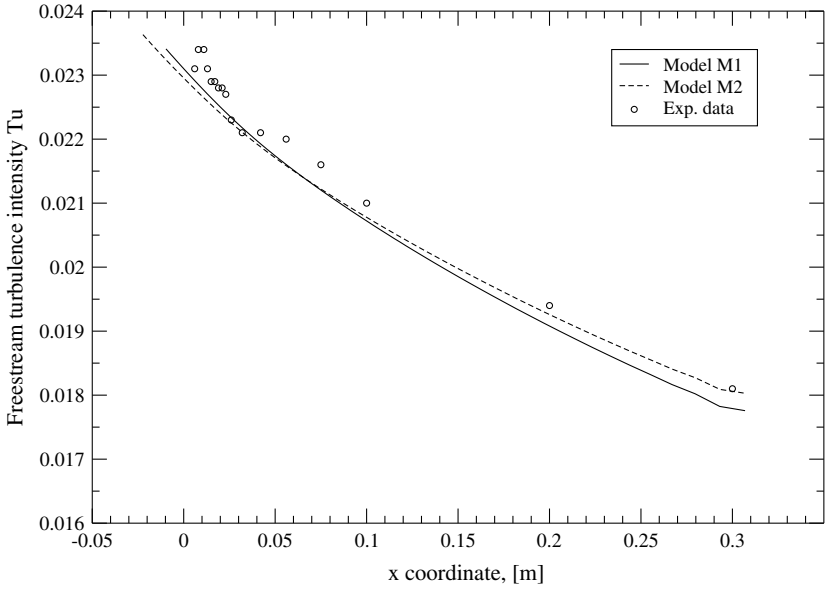

Fig. 4. T3L3 test case: free-stream turbulence intensity decay.

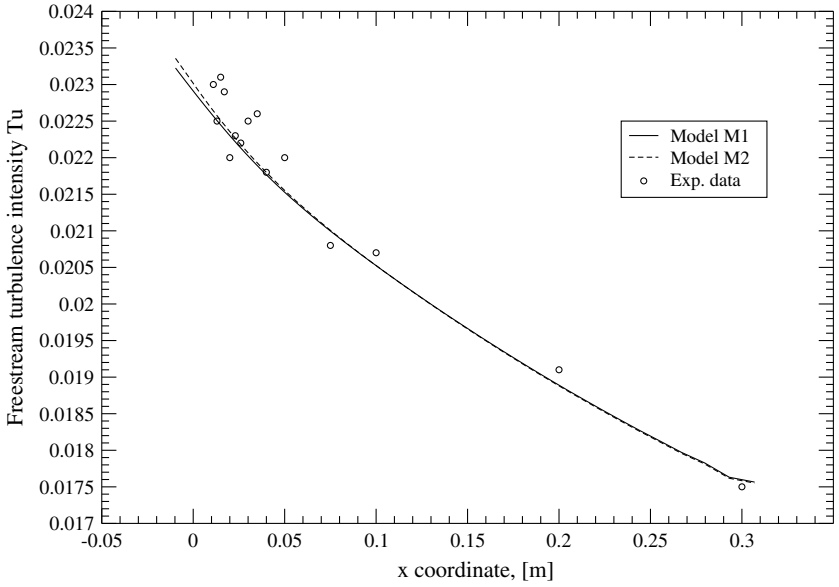

Fig. 5. T3L5 test case: free-stream turbulence intensity decay.

Table 3
Test cases T3L: separation, reattachment, and transition-onset points expressed in mm

Case	M1			M2			PR99		
	x_s	x_r	x_{to}	x_s	x_r	x_{to}	x_s	x_r	x_{to}
T3L2	4.70	28.9	18.0	4.70	27.0	24.0	4.66	29.1	24.1
T3L3	4.80	27.7	17.0	4.70	28.0	21.0	4.85	27.6	21.7
T3L5	5.00	40.0	41.0	5.10	39.8	38.1	5.00	38.3	41.6

rate parameter of the turbulent spots, v is the kinematic viscosity, and σ is the Emmons parameter (Emmons, 1951) which depends on the shape and velocity of the turbulent spots. In Eqs. (33) and (34) the spot production parameter $\hat{n}\sigma$ is computed as (Mayle, 1991)

$$\hat{n}\sigma = 1.510^{-11}\mathrm{Tu}_{\infty}^{7/4}, \tag{35}$$

where $\mathrm{Tu}_{\infty} = \mathrm{Tu}_{\mathrm{le},\infty}(u_{\mathrm{le},\infty}/u_{\infty})^{3/2}$ is the local free-stream value of Tu. In the presence of a pressure gradient, the correlation (35) for the spot production rate is corrected as

$$\hat{n}\sigma = (\hat{n}\sigma)_{\mathrm{ZPG}}\mathrm{PRC}, \tag{36}$$

where $(\hat{n}\sigma)_{\mathrm{ZPG}}$ is the production rate for zero pressure gradient (ZPG), Eq. (35), and PRC accounts for the influence of the pressure gradient through the value of the acceleration parameter K_{∞}

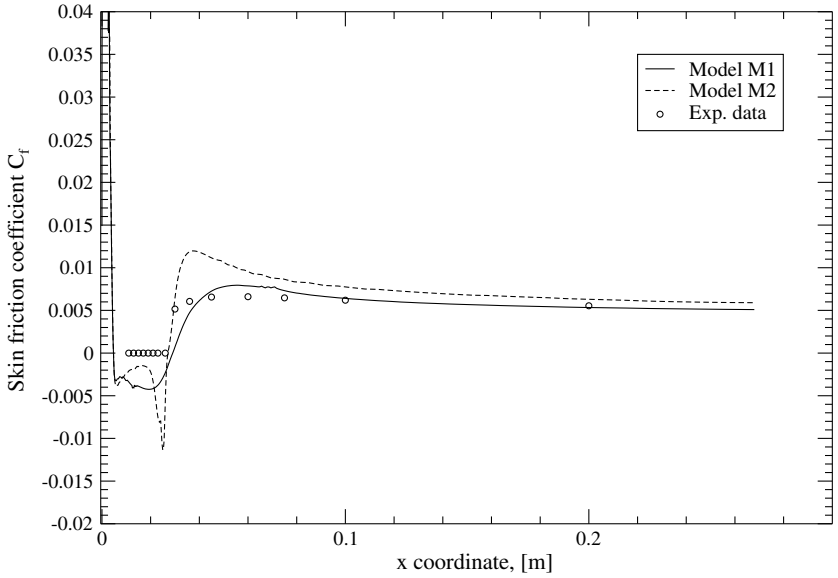

Fig. 6. Test case T3L2: skin friction coefficient distributions at the wall.

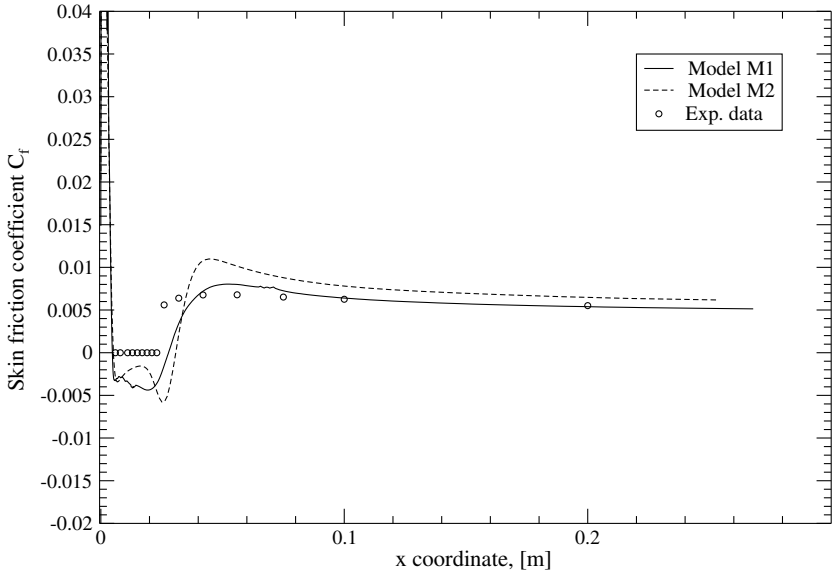

Fig. 7. Test case T3L3: skin friction coefficient distributions at the wall.

$$\mathrm{PRC} = \begin{cases} \left(474\mathrm{Tu}_{\mathrm{le}}^{-2.9}\right)^{1-\exp(2\times10^6 K_\infty)} & \text{for} \quad K_\infty < 0, \\ 10^{-3227K_\infty^{0.5985}} & \text{for} \quad K_\infty \geqslant 0, \end{cases} \tag{37}$$

where $\mathrm{Tu}_{\mathrm{le}}$ is the free-stream value of Tu at the leading-edge section. Eq. (37) has been obtained by Steelant and Dick (1996) from the data of Blair (1992) and Gostelow et al. (1994). The T_1, T_2 and T_3 terms in Eq. (30) are derived from the model of Cho and Chung (1992) and are given as

$$T_1 = \frac{C_1\gamma}{k}\tau_{ij}\frac{\partial u_i}{\partial x_j}, \tag{38}$$

$$T_2 = C_2\gamma\rho\frac{k^{1/2}}{\beta^*\omega}\frac{u_i}{\sqrt{u_k u_k}}\frac{\partial u_i}{\partial x_j}\frac{\partial \gamma}{\partial x_j}, \tag{39}$$

$$T_3 = C_3\rho\frac{k}{\beta^*\omega}\frac{\partial \gamma}{\partial x_j}\frac{\partial \gamma}{\partial x_j}. \tag{40}$$

Finally, the blending function, F, based on the correlation due to Klebanoff for the distribution of γ in the direction normal to the wall, is given as

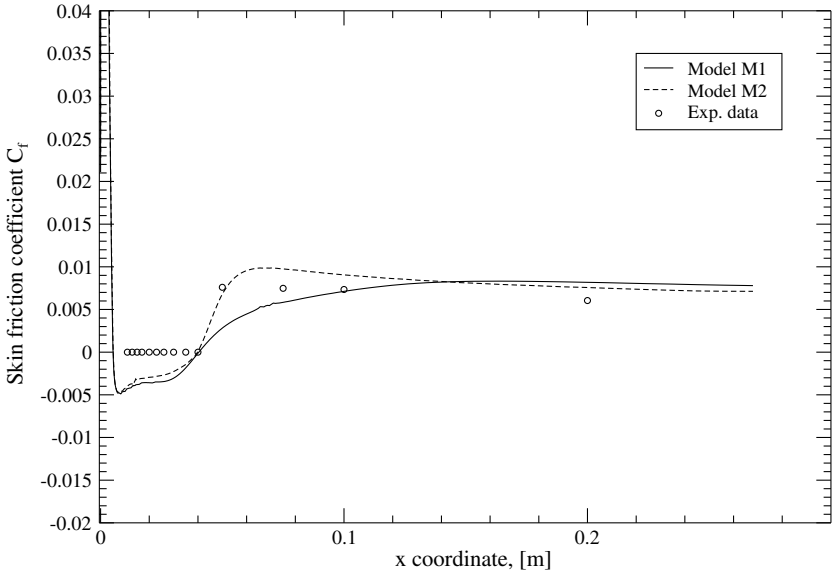

Fig. 8. Test case T3L5: skin friction coefficient distributions at the wall.

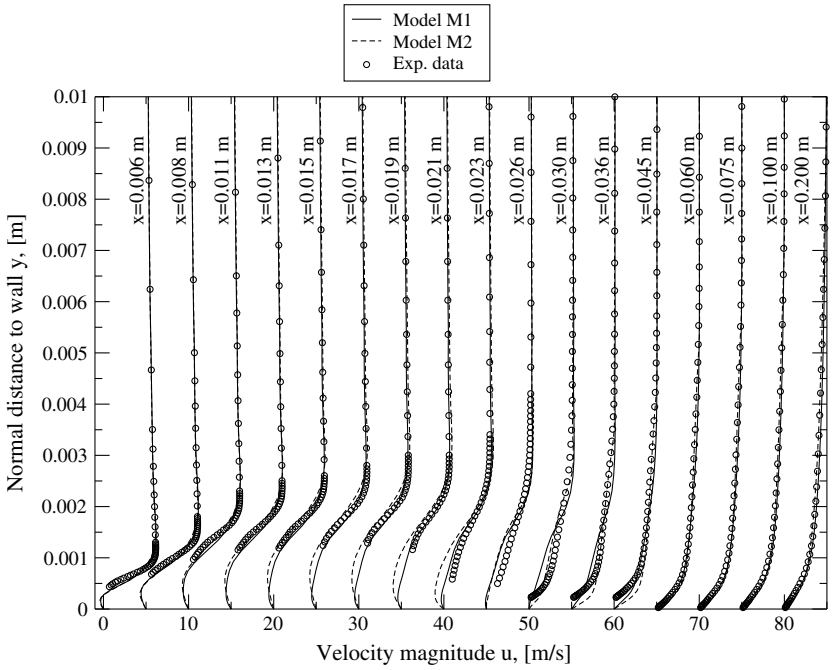

Fig. 9. T3L2 test case: velocity profiles.

$$F = \tanh^4\left[\frac{k/(Sv)}{200(1-\gamma^{0.1})^{0.3}}\right], \tag{41}$$

$$\begin{aligned} &\sigma_{\gamma_1} = 1, \quad \sigma_{\gamma_t} = 1, \\ &C_0 = 1, \quad C_1 = 1.6, \quad C_2 = 0.16, \quad C_3 = 0.15. \end{aligned} \tag{42}$$

which allows a smooth switch from the model of Steelant and Dick (1996) close to the wall to that of Cho and Chung (1992) in the outer region. The values of the coefficients in the equations above are

4. Numerical method

The numerical method employed to solve the three-dimensional RANS and transition model equations is the

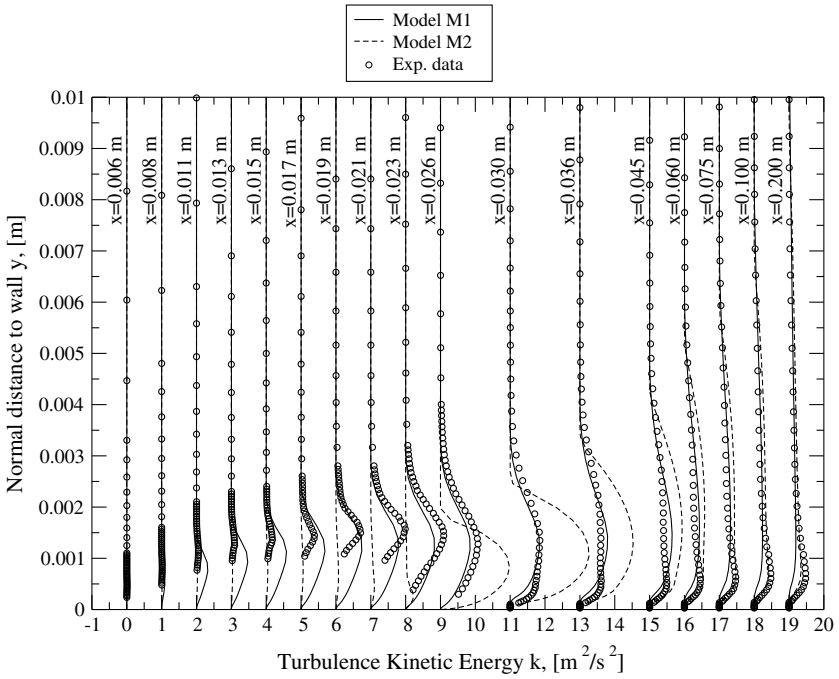

Fig. 10. T3L2 test case: turbulence kinetic energy profiles.

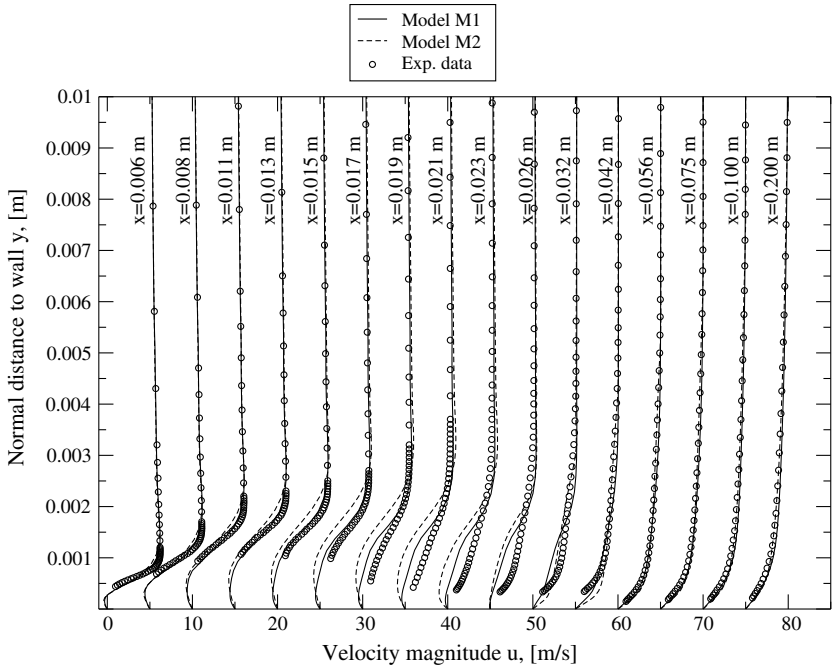

Fig. 11. T3L3 test case: velocity profiles.

extension to three space dimensions of the two-dimensional method of Cutrone et al. (2007). The conservation equations are written in generalized curvilinear coordinates; an implicit time marching procedure is used in combination with a preconditioning matrix (Venkateswaran et al., 1992; Merkle, 1995), premultiplying the pseudo-time derivative, in order to improve accuracy and efficiency for a wide range of the Mach number. Using the diagonalization procedure of Pulliam and Chaussee (1981), it is possible to factorize the implicit operator, so as to allow a standard scalar alternating direction implicit solution procedure (Buelow et al., 1997). A cell-centred finite volume space discretization is used on a multi-block structured mesh. The third-order-accurate Steger and Warming (1981) flux vector splitting scheme is employed to discretize the convective terms, whereas the viscous terms are discretized by

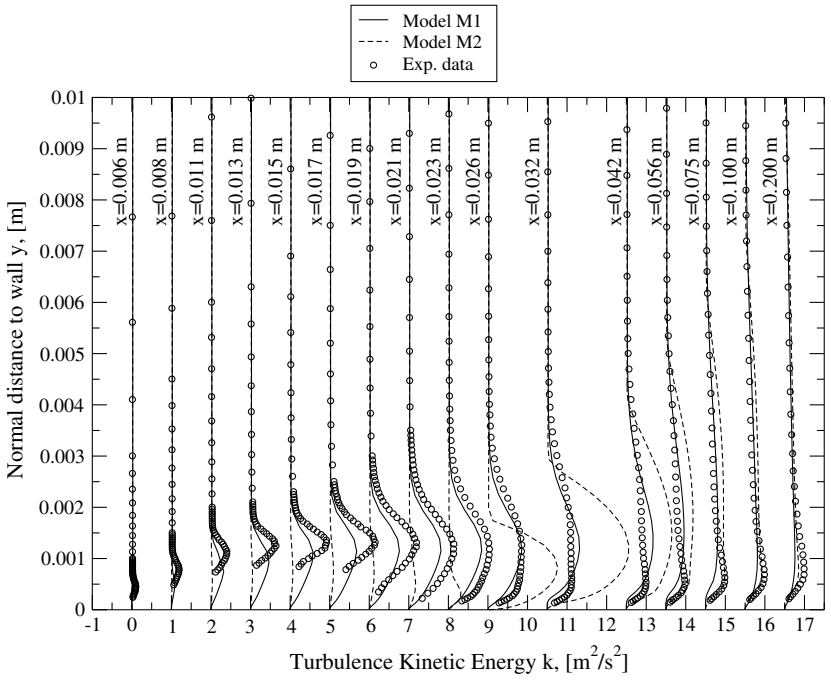

Fig. 12. T3L3 test case: turbulence kinetic energy profiles.

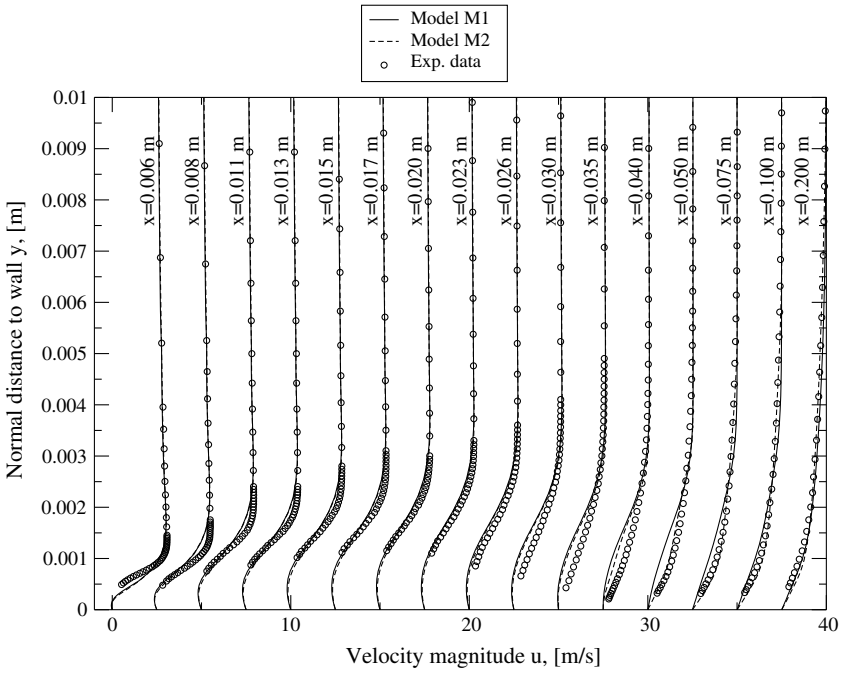

Fig. 13. T3L5 test case: velocity profiles.

second-order-accurate central differences. Characteristic boundary conditions for the flow variables are imposed at inflow and outflow points, whereas no-slip and adiabatic conditions are imposed at walls; k and ω are assigned at inflow points together with $\gamma = 0$, whilst they are linearly extrapolated at outflow points. At solid walls, k is set to zero whereas different conditions have been employed for ω, namely: (i) the homogeneous Neumann condition, $\partial\omega/\partial n = 0$, which was found adequate for model M1 in the case of attached flows (Walters and Leylek, 2005; Cutrone et al., 2007); (ii) the condition proposed by Menter and Rumsey (1994),

$$\omega = 60\frac{\nu}{y_{n,1}^2\beta}, \tag{43}$$

where $y_{n,1}$ is the distance of the first cell center from the wall; (iii) a combination of (i) and (ii), see Section 5.

All results have been obtained using double-precision arithmetic; the computations are started impulsively from rest, the turbulence and transition quantities being all set to zero. A residual drop of eight orders of magnitude for the conservation-law Eqs. (1)–(3) has been required for convergence.

5. Results

As already mentioned in the Introduction, this work aims at evaluating the Walters and Leylek (2004) model for predicting transition in turbomachinery flows. Preliminarily, flows past a flat plate tested at the Rolls-Royce Applied Science Laboratory wind tunnel with different free-stream conditions, known as T3L test cases (available on the web at http://ercoftac.mech.surrey.ac.uk/transition/cases), have been used to test such a model versus well-documented two-dimensional transitional separated flows. For such cases, results have also been obtained using the Suzen and Huang (2000) model, for comparison.

5.1. T3L test cases

The first test case is one of the experimental tests performed by the ERCOFTAC Special Interest Group (SIG) on Transition (Savill, 1993a,b): the flow past a flat plate with a semi-circular leading edge having radius equal to 5 mm, incidence angle and pressure gradient both equal to zero, and several free-stream conditions. The computational domain, $x_{\min} = -0.3$ m, $x_{\max} = 0.3$ m, $y_{\min} = 0$, $y_{\max} = 0.218$ m, is shown in Fig. 2 along with a partial view of the grid at the leading-edge region. Along the lower wall, upstream of the plate leading-edge, inviscid wall boundary conditions are imposed, whereas at the plate as well as at

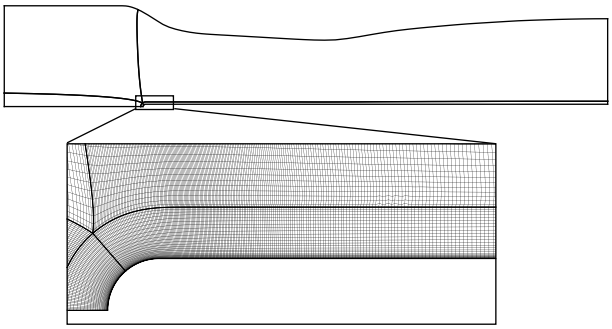

Fig. 15. T3LA1 test case: computational domain and partial view of the grid at the leading-edge region.

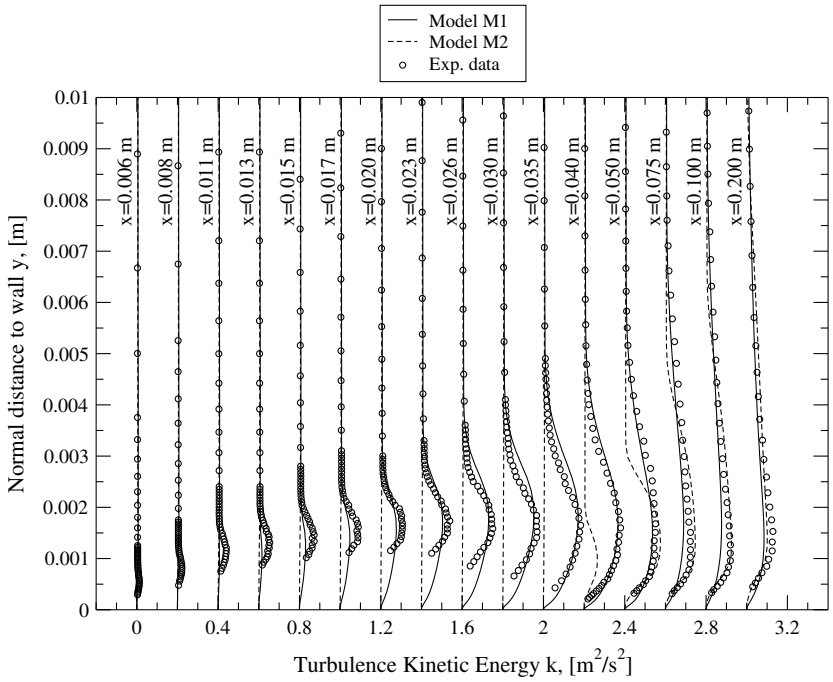

Fig. 14. T3L5 test case: turbulence kinetic energy profiles.

the upper wall the no-slip condition is enforced. The grid is composed of five blocks and contains about 35,000 cells; a near-wall clustering allows y^+ for the first cell as low as 0.01. The three flow conditions provided in Table 1 have been computed, the free-stream velocity, u_∞, Reynolds number, Re (based on the leading-edge diameter), and turbulence intensity, Tu_∞, referring to the test section, located 6 mm downstream of the leading-edge. In order to recover such experimental data, at the inlet section of the computational domain, the values u_{in}, Tu_{in}, and $\lambda_{T,in}$ have been assigned as given in Table 2, which also provides the numerical (n) and experimental (exp) turbulence length scales at the test section. A satisfactory agreement between the computed and experimental decays of the free-stream turbulence intensity is also obtained, see Figs. 3–5. The flow always separates near the start of the plate (the end of the nose), the length of the separation bubble varying between 2.5 and 3 times the leading-edge diameter, and transition onset occurs before or just after the reattachment point; see Table 3, which provides the x-coordinates of the separation (s), reattachment (r), and transition-onset (to) points, computed using both models M1 and M2, together with the numerical results of Papanicolaou and Rodi (1999). For model M1, the x_{to} value has been evaluated according to one of the transition-onset criteria commonly employed in experimental works, see, e.g., Hoheisel et al.

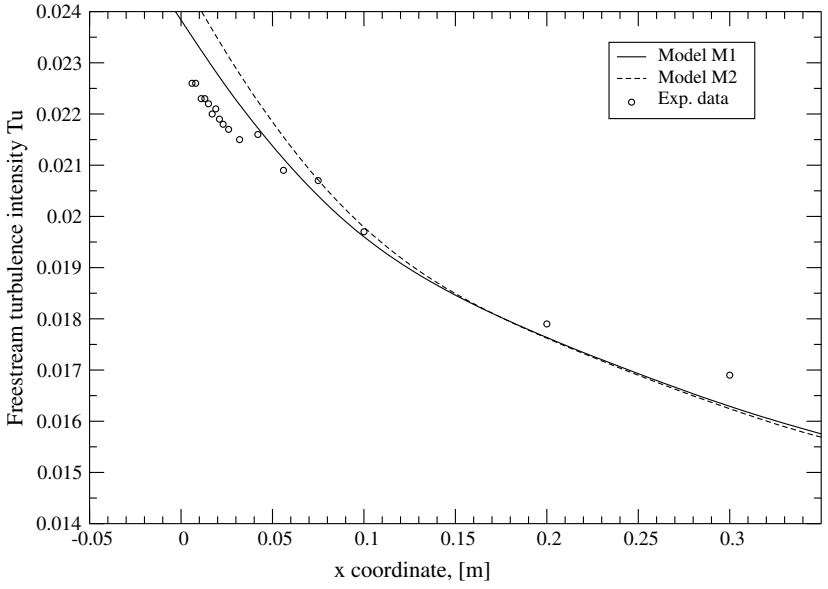

Fig. 16. T3LA1 test case: free-stream turbulence intensity decay.

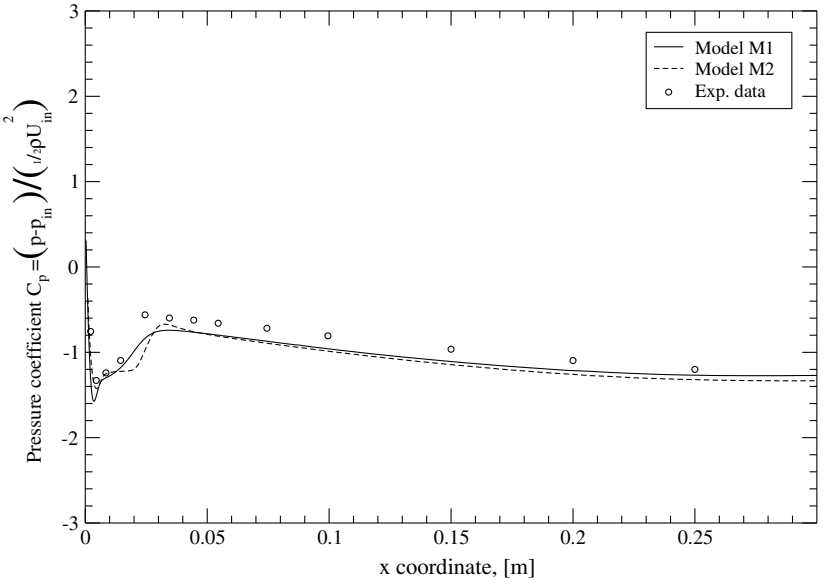

Fig. 17. T3LA1 test case: pressure coefficient distributions at the wall.

(1987), Schlichting (1968): transition onset occurs at the point where the ratio between the dynamic pressures at a distance $\tilde{y}$ from the wall and at the edge of the boundary-layer,

$$\frac{q(x,\tilde{y})}{q(x,\delta)} = \frac{p_t(x,\tilde{y}) - p(x,\tilde{y})}{p_t(x,\delta) - p(x,\delta)}, \tag{44}$$

reaches its minimum along the wall; here $\tilde{y} = 1$ mm. This criterion was not necessary for model M2 as well as for the results of Papanicolaou and Rodi (1999), which determine the transition onset, directly. The skin friction coefficients, computed using either model, are compared with the experimental ones in Figs. 6–8. Model M1 provides adequate results; in particular, it predicts correctly the T3L5 test case where, unlike the other ones, the transition onset occurs just downstream of the reattachment point, as also predicted by the results of Papanicolaou and Rodi (1999). Model M2 is less robust, insofar as it provides results comparable with those of model M1, except for the undershoot and overshoot just upstream and downstream of the reattachment point, respectively, for both cases T3L2 and T3L3.

A more thorough comparison of the present results with the experimental ones is shown in Figs. 9–14, which pro-

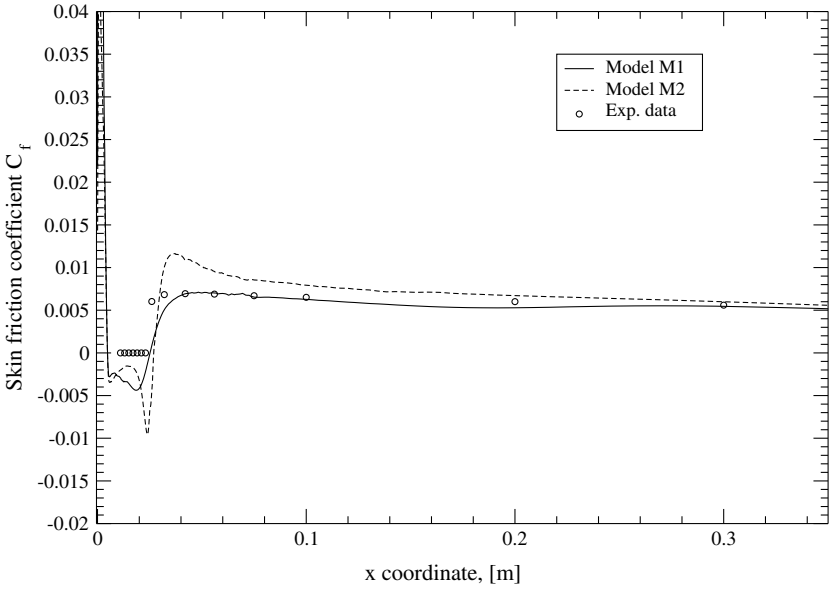

Fig. 18. T3LA1 test case: skin friction coefficient distributions at the wall.

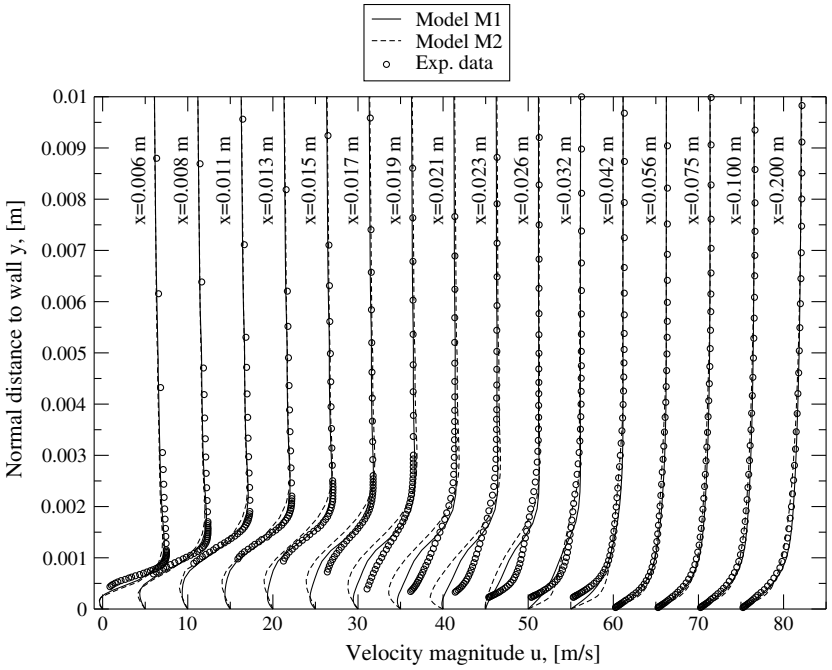

Fig. 19. T3LA1 test case: velocity profiles.

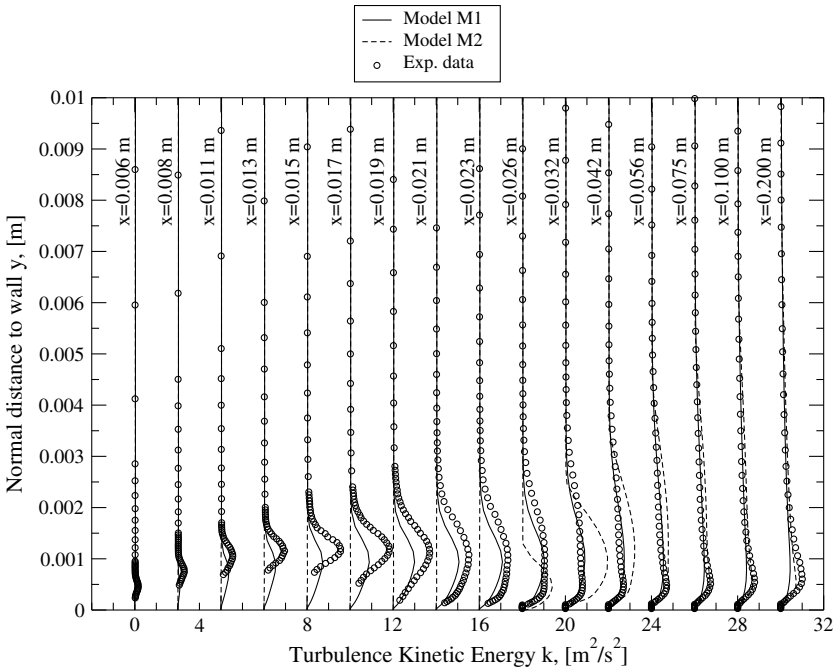

Fig. 20. T3LA1 test case: turbulence kinetic energy profiles.

Table 4
Test case T3L3: mesh-refinement study

	Grid A	Grid B	Grid C
Number of cells	35,000	17,000	9000
Points in the boundary-layer	32	23	16
$y_{n,1}$	10^{-6}	10^{-5}	5×10^{-5}
$y^+_{n,1}$	0.01	0.08	0.65
x_r(mm) – M1	27.7	27.3	26.2
x_r(mm) – M2	28.0	28.0	30.0

vide the velocity and turbulence kinetic energy profiles at different locations along the plate. The agreement is generally good, except near the reattachment point where the largest errors are experienced, markedly by model M2 in the T3L2 and T3L3 cases. Such errors are likely due to those relative to the production of the turbulence kinetic energy, k. On one hand, model M1 overpredicts the production of k near the wall, for case T3L2, and underpredicts it near transition for case T3L3, while always capturing its correct profile across the bubble both before and after transition onset. This is in agreement with experimental data of Malkiel and Mayle (1996), which show that the point of maximum intermittency, and hence that of maximum turbulence production, coincides with the point of maximum vorticity, corresponding to the center of the

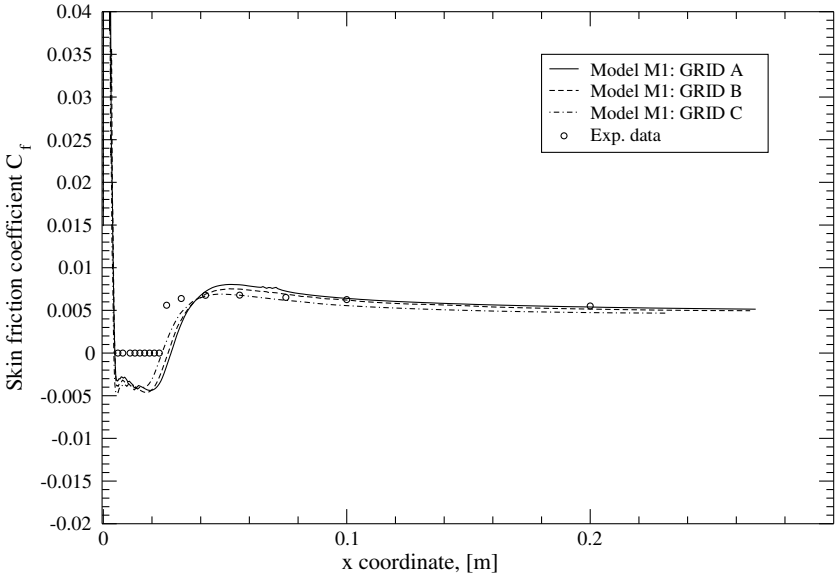

Fig. 21. Mesh-refinement study for model M1: skin friction coefficient distributions at the wall for test case T3L3.

separation bubble. On the other hand, model M2 is not able to predict the pre-transitional kinetic energy production, due to its on/off transition-onset criterion; consequently, the corresponding turbulence kinetic energy profiles differ from zero only downstream of transition onset and are markedly less accurate that those provided by model M1.

It is noteworthy that model M2 is not able to provide separation when used in conjunction with Menter's wall boundary condition for ω in the entire flow-field, so that the *mixed* condition has been employed, using Menter's Eq. (43) only after the reattachment point and the homogeneous Neumann condition elsewhere. Such a condition was used also for model M1. However, it has been observed that the results of model M1 are only slightly dependent on the condition used for ω at walls. In particular, for the test case T3L3, the reattachment point obtained using either Menter's boundary condition or the Neumann one is equal to 28.2 mm, only about 1.8% different with respect to the value obtained using the *mixed* condition.

The T3LA1 test case has been also considered, which differs from the previous ones only for the presence of an upper wall (uw), imposing a non-zero pressure gradient along the flat plate. $Re = 3293$ and the computational domain, $x_{min} = -0.3$ m, $x_{max} = 1$ m, $y_{min} = 0$, $y_{max} = y_{uw}$, is shown in Fig. 15 along with a partial view of the grid at the leading-edge region. The grid is composed of five blocks and contains about 38,000 cells; a near-wall clustering allows y^+ for the first cell as low as 0.01. The turbulence intensity and length scale imposed at the inlet points are equal to 3.9% and 14.1 mm, which allowed a good agreement between the computed and the experimental free-stream turbulence intensity decays, see Fig. 16. Figs. 17 and 18 provide a comparison between the computed and experimental pressure and skin friction coefficient distributions along the plate, respectively, showing a good agreement. The computed separation, reattachment, and transition-onset points are equal to $x_s = 4.7$ mm, $x_r = 25.1$ mm, and $x_{to} = 15.0$ mm, for model M1, and $x_s = 4.6$ mm, $x_r = 26.5$ mm, and $x_{to} = 21.2$ mm (17.5 mm, if using Eq. (44)), for model M2. Figs. 19 and 20 finally provide the velocity and turbulence kinetic energy profiles: all results confirm those of the previous test cases.

Finally, a mesh-refinement study has been performed in order to demonstrate that all of the results presented so far can be considered to be *grid-converged* within plotting accuracy. In order to save computational effort, the mesh-refinement study has been performed only for one test case (T3L3) and coarsening twice the initial mesh (grid

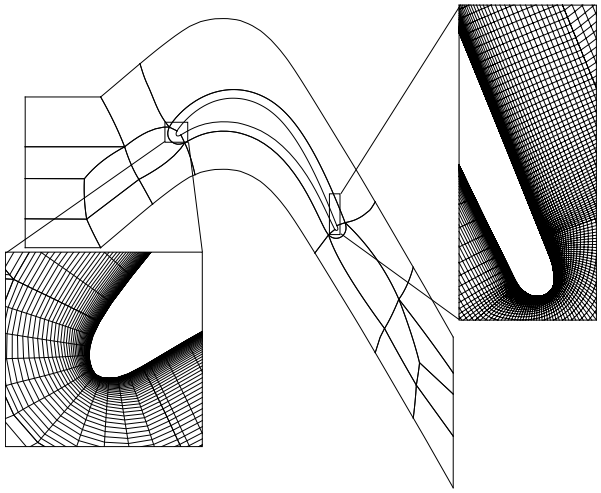

Fig. 23. T106 test case: computational domain and partial view of the grid at the leading- and trailing-edge regions.

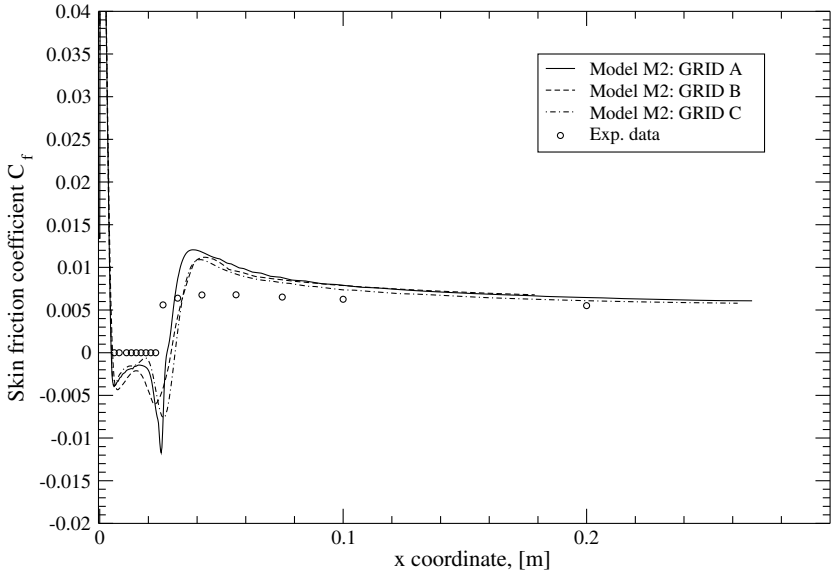

Fig. 22. Mesh-refinement study for model M2: skin friction coefficient distributions at the wall for test case T3L3.

A). Table 4 provides the main features of the grids as well as the computed locations of the reattachment point, whereas Figs. 21 and 22 provide a comparison of the skin friction coefficient distributions. It appears that already grid B can be considered adequate for the present computations, especially for model M1, which again proves to be more robust than model M2.

From all results, it appears that model M1 is more reliable and robust than model M2. Furthermore, it is also easier to apply to complex geometries and three space dimensions, insofar as it does not require to evaluate any nonlocal parameter such as a boundary-layer thickness. Therefore, model M1 appears as the ideal candidate for predicting transition in two- and three-dimensional separated flows of turbomachinery interest, and deserves further testing, as done in the following.

5.2. Two-dimensional flow through the T106 turbine cascade

The two-dimensional flow through the T106 turbine cascade has been computed to validate the transition model M1 versus a turbomachinery flow with separation-induced transition (Hoheisel et al., 1987). The flow is subsonic, with isentropic exit Mach number equal to 0.59, inlet flow angle equal to 37.7°, and inlet turbulence length scale equal to $0.02c$, c being the chord length, equal to 100 mm. Two

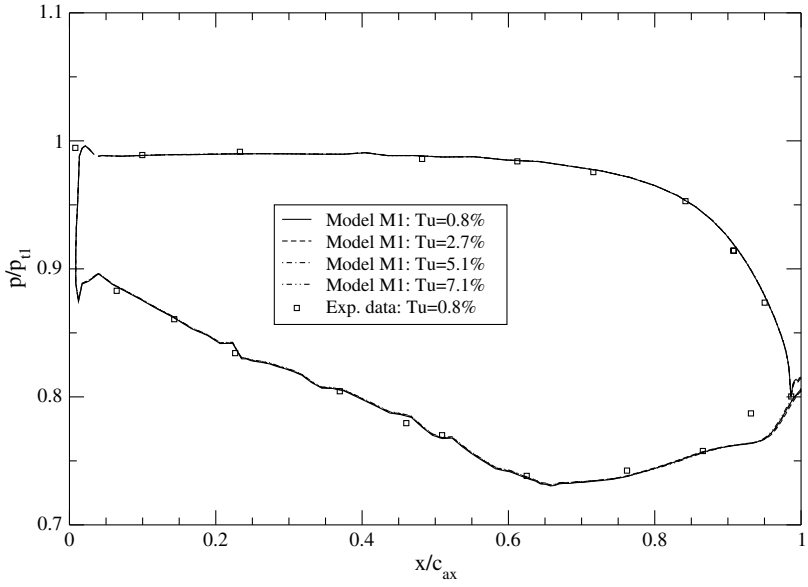

Fig. 24. T106 test case, $Re = 5 \times 10^5$: pressure coefficient distributions at the wall.

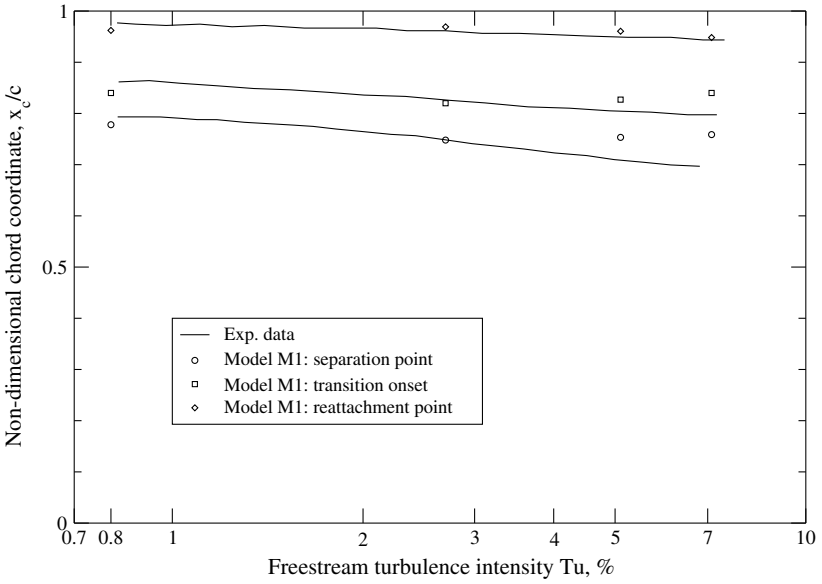

Fig. 25. T106 test case, $Re = 5 \times 10^5$: separation, transition-onset, and reattachment points versus inlet turbulence intensity.

values of the Reynolds number, based on c and on the exit conditions, have been considered, namely, 5×10^5 and 11×10^5. Experiments by Hoheisel et al. (1987) indicate that, for the lower Re, separated-flow transition occurs for values of the inlet turbulence intensity Tu in the range $0.8\% \leqslant \mathrm{Tu} \leqslant 7.1\%$, whereas, for the higher Re, separated-flow transition occurs only for $\mathrm{Tu} \leqslant 3\%$, an attached bypass transition being observed for $\mathrm{Tu} > 3\%$.

The inlet and outlet sections of the computational domain are located at a distance equal to s and $0.875s$ upstream of the leading-edge and downstream of the trailing-edge sections, respectively, s being the cascade pitch, equal to 79.9 mm. The computational domain is shown in Fig. 23 along with a partial view of the grid at the leading- and trailing-edge regions. The grid is composed of 24 blocks and contains about 68,800 cells; a near-wall clustering allows y^+ for the first cell as low as 0.05. This grid accurately captures the features of the present flow, as already shown by De Palma (2002). The transition-onset location is evaluated according to Eq. (44), with $\tilde{y} = 0.15$ mm.

For $Re = 5 \times 10^5$, Fig. 24 provides the experimental and computed distributions of the nondimensional pressure along the blade profile. The numerical results, independent of Tu, agree well with the experimental ones, but overesti-

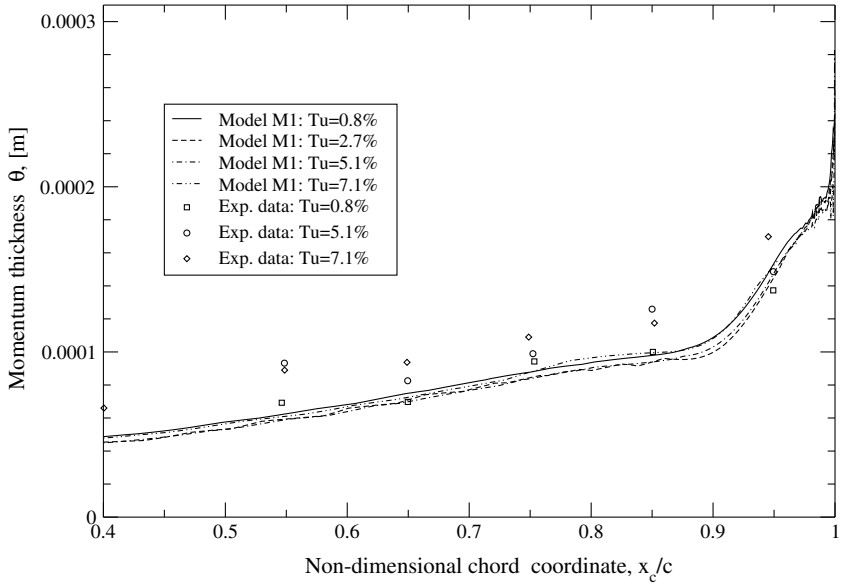

Fig. 26. T106 test case, $Re = 5 \times 10^5$: momentum thickness distributions along the suction side.

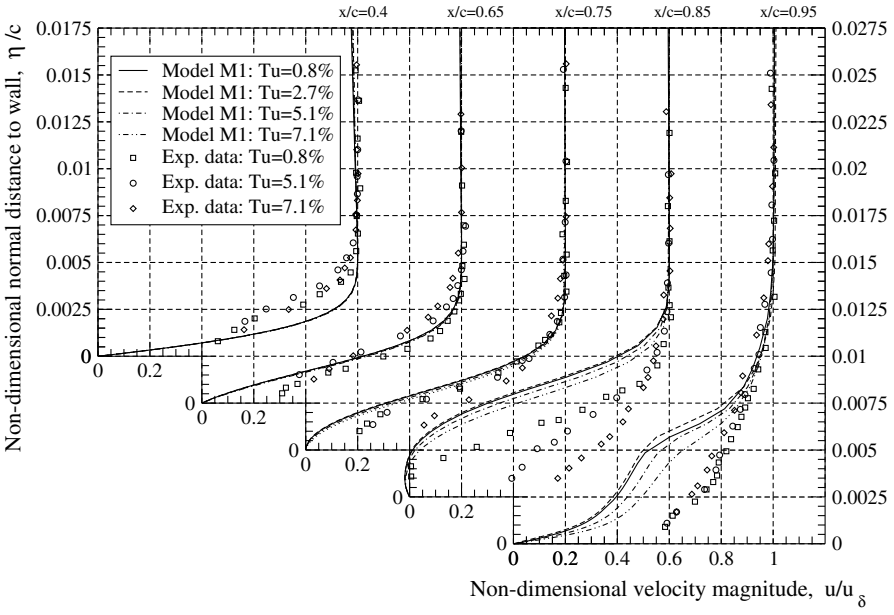

Fig. 27. T106 test case, $Re = 5 \times 10^5$: velocity profiles.

mate the pressure plateau due to the separation bubble at the rear suction side. Fig. 25 provides the experimental and numerical values of the separation, transition-onset and reattachment points versus the inlet turbulence intensity. The agreement of the two sets of data is satisfactory, the separation and transition-onset points being slightly over-predicted for the two highest values of Tu. Fig. 26 provides the distributions of the boundary-layer momentum thickness along the blade suction side. The flow remains laminar over a large portion of the blade suction side, a laminar separation bubble taking place at about 70–80% of the chord, depending on the inlet Tu value; transition occurs at the edge of the separation bubble, and a fully turbulent flow reattaches at $x/c \cong 0.94$. The computed and experimental boundary-layer velocity profiles at five locations along the suction side are finally given in Fig. 27. The velocity profiles at $x/c = 0.75$ indicate a tendency toward separation, which is evident at $x/c = 0.85$. The numerical results for the last two locations do not compare particularly well with the experimental data: at $x/c = 0.85$, the computed profiles are weakly dependent on Tu and appear closer to the experimental data

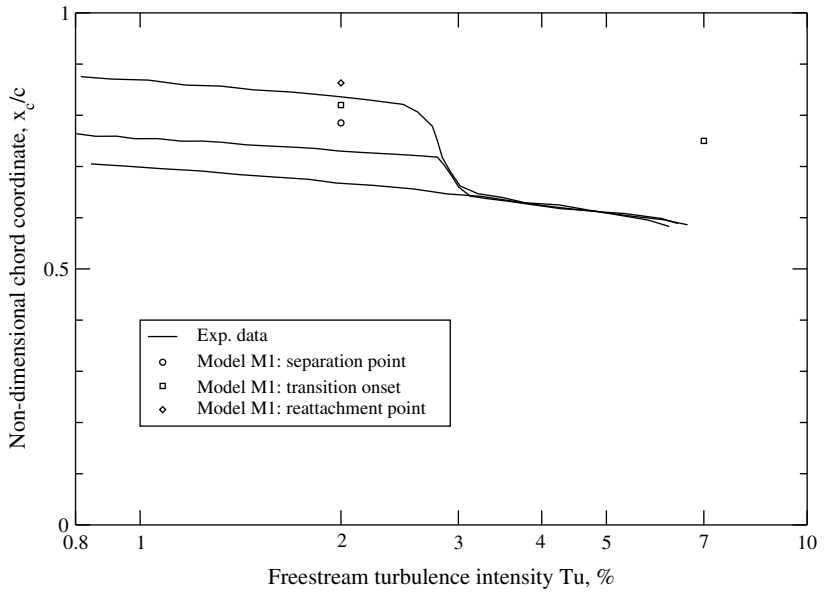

Fig. 28. T106 test case, $Re = 11 \times 10^5$: separation, transition-onset, and reattachment points versus inlet turbulence intensity.

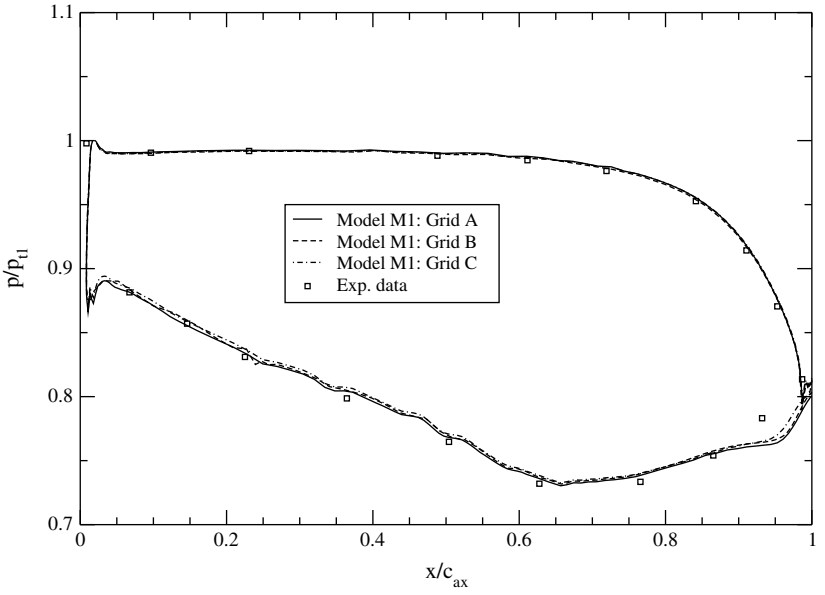

Fig. 29. T106 3D test case: pressure coefficient distributions at mid-span.

corresponding to Tu = 0.8%; at $x/c = 0.95$, the behaviour is opposite and the computed profiles are not fully turbulent, unlike the experimental ones. However, it is somewhat surprising that the experiments show a well developed attached turbulent velocity profile at $x/c = 0.95$, reattachment taking place at $x/c \cong 0.94$.

For $Re = 11 \times 10^5$, two values of Tu have been considered, namely, 2% and 7%. Also for such cases, model M1 is able to predict the separated-flow transition for the lower Tu, as shown in Fig. 28, although less accurately than in the previous case; more importantly, for the higher Tu, the model correctly predicts that there is no separation and an attached bypass transition occurs.

5.3. Three-dimensional flow through the T106 turbine linear cascade

The three-dimensional flow through the same linear T106 turbine cascade has been finally considered to validate the transition model M1 versus a complex turbomachinery flow involving separation, transition, and their interactions with secondary flows, a very challenging test for transitional-flow solvers (De Palma, 2002; Hildebrandt and Fottner, 1999). The flow is subsonic with: isentropic exit Mach number equal to 0.59, inlet flow angle equal to 37.7°, Reynolds number, based on c and on the exit conditions, equal to 5×10^5, and inlet turbulence length scale

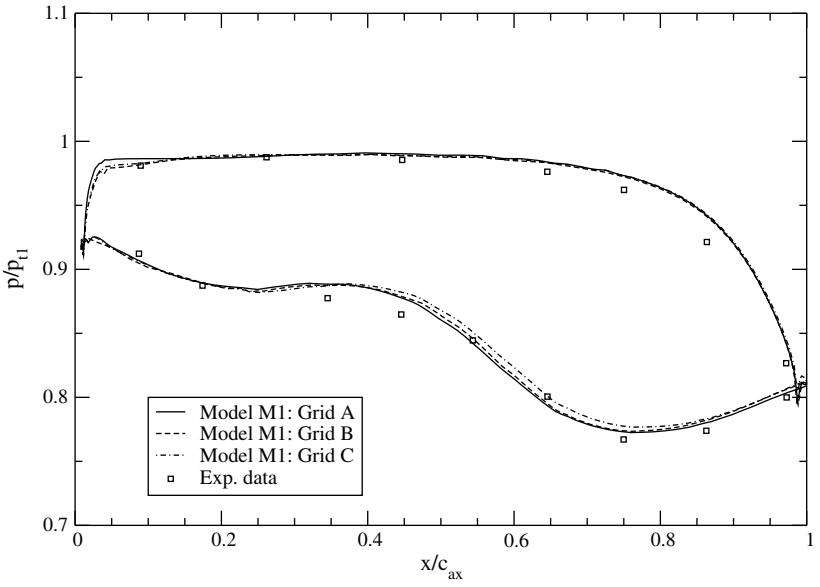

Fig. 30. T106 3D test case: pressure coefficient distributions at the sidewall.

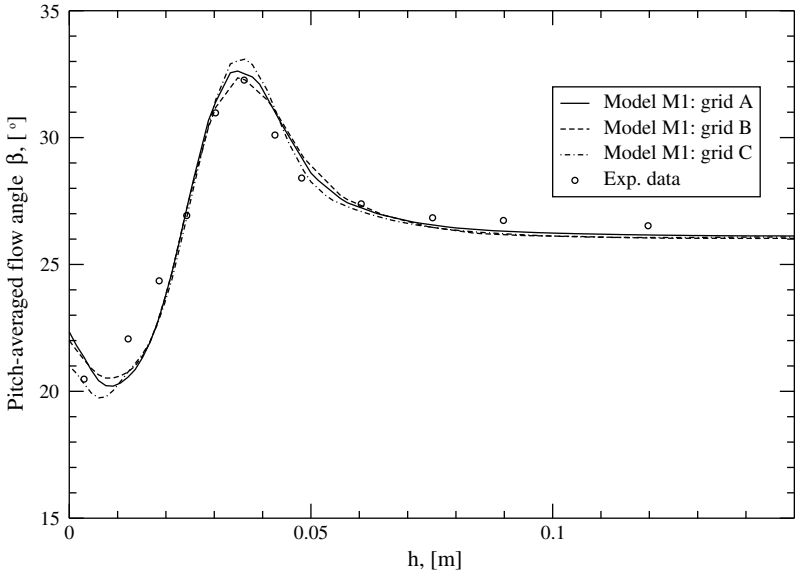

Fig. 31. T106 3D test case: pitch-averaged flow angle variations along the span downstream of the cascade.

equal to $0.02c$. The inlet turbulence intensity has been set equal to 5.8% and the measured total-pressure spanwise profile has been prescribed at inlet points, in order to compare the results with the experimental data of Hildebrandt and Fottner (1999).

The inlet and outlet sections of the computational domain are located like in the previous test case and the third dimension has been simulated from hub to mid-span ($h = 150$ mm) due to symmetry. Three grids with 24 blocks have obtained by stacking a two-dimensional grid in the blade passage non-uniformly in the spanwise direction. The grids contain about $14,600 \times 40$ cells (grid A), $36,500 \times 48$ cells (grid B), and $14,600 \times 80$ (grid C), respectively, so as to have values of y^+ for the first cell at the blade wall about equal to 0.2, 0.1, and 0.2, and of z^+ for the first cell at the hub equal to 1, 0.9 and 0.25, respectively. The computed nondimensional pressure distributions at the mid-span and sidewall sections are compared with the experimental ones in Figs. 29 and 30, respectively. The behaviour at mid-span, where the flow can be considered two-dimensional, recovers that of Fig. 24, and the agreement at the sidewall, where complex three-dimensional features are present, is remarkable indeed. In both cases the numerical results are just about grid-converged.

In order to assess the capability of the model to predict secondary flows, the pitchwise averages of the exit flow angle and of the loss coefficient at the plane $x/c_{ax} = 1.5$ have been computed and compared with the experimental data in Figs. 31 and 32, respectively. Considering the complexity of the flow, the grid dependency is small and the agreement is good. The details of the flow downstream of the cascade are given in Fig. 33, which provides the contours of the loss coefficient at the plane $x/c_{ax} = 1.5$: a large two-dimensional flow region extends from mid-span

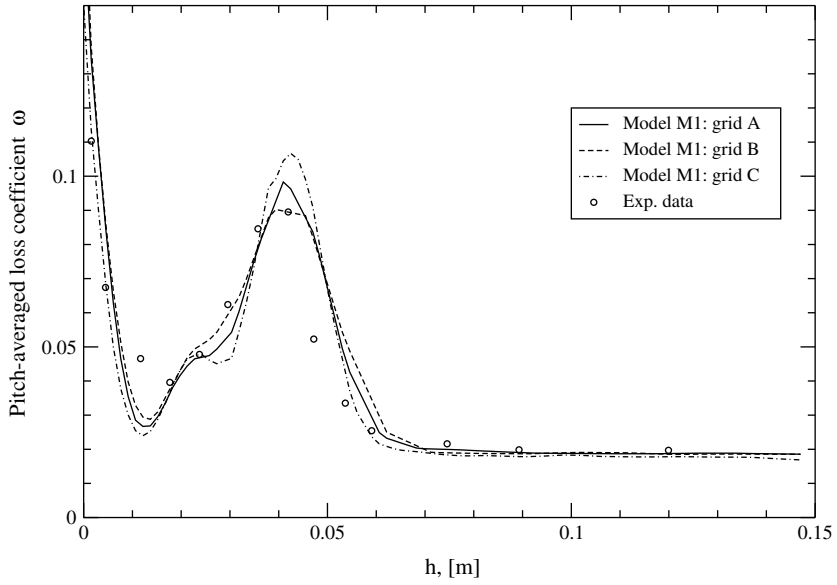

Fig. 32. T106 3D test case: pitch-averaged loss coefficient variations along the span downstream of the cascade.

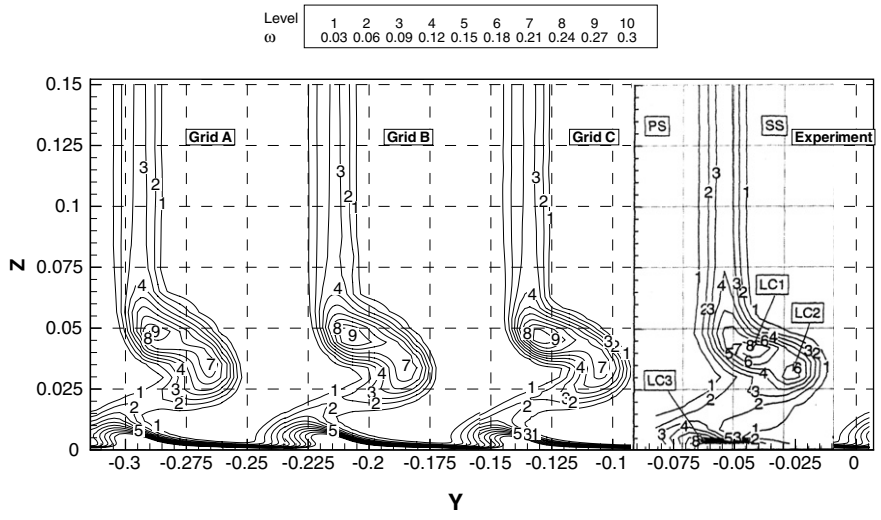

Fig. 33. T106 3D test case: loss coefficient at $x/c_{ax} = 1.5$.

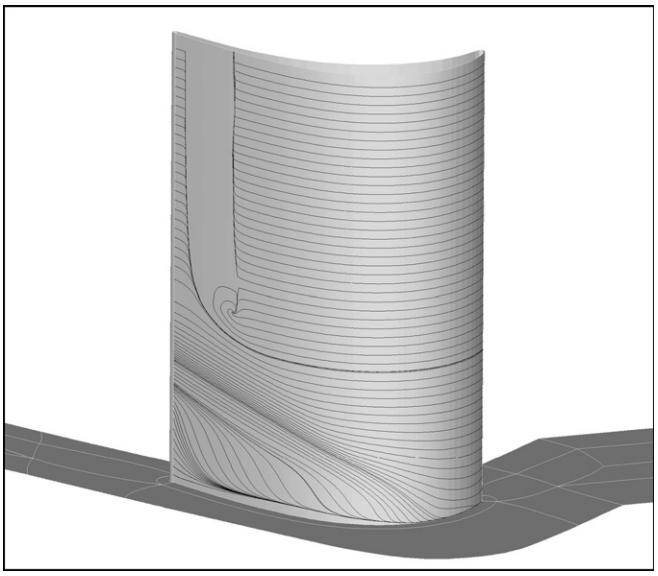

Fig. 34. T106 3D test case: limiting streamlines on the suction surface.

($h = 150$ mm) to about 75 mm from the sidewall. Three different loss cores (LC) are clearly seen (Hildebrandt and Fottner, 1999). The main one, LC1, originates between the separation lines of the suction side branch of the horseshoe vortex and of the passage vortex; LC2 is directly related to the passage vortex; and LC3 is due to the corner vortex, which is induced by the passage vortex and counter-rotates with respect to it. All such features are well captured by the numerical simulations; more importantly, the losses computed on the three grids are in good agreement among themselves as well as with the experimental data. This is a very important result, insofar as numerical simulations employing a RANS approach and a transition model usually overpredict losses and are very sensitive to the mesh (Hildebrandt and Fottner, 1999; De Palma, 2002). Finally, Fig. 34 provides the limiting streamlines on the blade suction side (computed using grid C), showing that a separation bubble is present at the aft suction surface of the blade, from mid-span to about 75 mm, consistently with the loss coefficient contours.

6. Conclusions

In this work, transition in two- and three-dimensional separated flows has been studied numerically in order to assess the performance of the single-point transition model recently proposed by Walters and Leylek (2004). This model, called M1, is based on the computation of the pre-transitional stream-wise boundary-layer fluctuations induced by the free-stream turbulence, through the solution of an additional transport equation for the laminar kinetic energy. Unlike standard intermittency transport models, M1 does not require to evaluate any nonlocal parameter and is thus suitable for computing complex three-dimensional flows. Firstly, model M1 as well as a second state-of-the-art model (M2), combining a transition-onset correlation with an intermittency transport equation, have been tested versus well-documented incompressible flows past a flat plate with semi-circular leading edge, namely, tests T3L2, T3L3, T3L5, and T3LA1 of ERCOFTAC, the last one being characterized by a non-zero pressure gradient. In all cases, model M1 has proven itself more reliable and accurate than its competitor. Then, it has been tested versus the two- and three-dimensional flows through the T106 linear turbine cascade, for which detailed experimental results are available. Also for such very complex and challenging flows, model M1 has proven to be robust and accurate. Model M1 is thus a suitable candidate to be a crucial ingredient within a state-of-the-art CFD tool for transitional turbomachinery flows based upon the RANS equations and the low-Reynolds-number $k - \omega$ turbulence model.

Acknowledgement

This research has been supported by the MiUR and the Politecnico di Bari, Grant CofinLab 2000 (CEMeC).

References

Abe, K., Jang, Y.-J., Leschziner, M.A., 2003. An investigation of wall-anisotropy expression and length-scale equations for non-linear eddy-viscosity models. Int. J. Heat Fluid Flow 24, 181–198.

Blair, M.F., 1992. Boundary-layer transition in accelerating flows with intense freestream turbulence: Part 2 – The zone of intermittent turbulence. ASME J. Turbomach. 114, 322–332.

Buelow, P.E.O., Schwer, D.A., Feng, J.-Z., Merkle, C.L., Choi, D., 1997. A preconditioned dual time diagonalized ADI scheme for unsteady computations. AIAA Paper 97-2101.

Chen, W.L., Lien, F.S., Leschziner, M.A., 1998. Non-linear eddy-viscosity modelling of transitional boundary layers pertinent to turbomachine aerodynamics. Int. J. Heat Fluid Flow 19, 297–306.

Cho, R., Chung, M.K., 1992. A $k - \epsilon - \gamma$ equation turbulence model. J. Fluid Mech. 237, 301–322.

Craft, T.J., Launder, B.E., Suga, K., 1997. Prediction of turbulent transitional phenomena with a nonlinear eddy-viscosity model. Int. J. Heat Fluid Flow 18, 15–28.

Cutrone, L., De Palma, P., Pascazio, G., Napolitano, M., 2007. An evaluation of bypass transition models for turbomachinery flows. Int. J. Heat Fluid Flow 28, 161–177.

De Palma, P., 2002. Accurate numerical simulation of compressible turbulent flows in turbomachinery. AIAA J. 40, 702–708.

De Palma, P., 2006. Numerical simulations of three-dimensional transitional compressible flows in turbomachinery cascades. Int. J. Numer. Meth. Heat Fluid Flow 16, 509–529.

Dhawan, S., Narasimha, R., 1958. Some properties of boundary layer during the transition from laminar to turbulent flow motion. J. Fluid Mech. 3, 418–438.

Durbin, P.A., 1996. On the k–ϵ stagnation point anomaly. Int. J. Heat Fluid Flow 17, 89–90.

Emmons, H.W., 1951. The laminar-turbulent transition in a boundary layer – Part I. J. Aerosol. Sci. 18, 490–498.

Gostelow, J.P., Blunden, A.R., Walker, G.J., 1994. Effects of free-stream turbulence and adverse pressure gradients on boundary layer transition. ASME J. Turbomach. 116, 392–404.

Hanialić, K., Jakirlić, S., Hadzić, I., 1997. Expanding the limits of "equilibrium" second-moment turbulence closures. Fluid Dyn. Res. 20, 25–41.

Hildebrandt, T., Fottner, L., 1999. A numerical study of the influence of grid refinement and turbulence modeling on the flow field inside a highly loaded turbine cascade. ASME J. Turbomach. 121, 709–716.

Hodson, H.P., Howell, R.J., 2005. Bladerow interactions, transition, and high-lift aerofoils in low-pressure turbines. Annu. Rev. Fluid Mech. 37, 71–98.

Hoheisel, H., Kiock, R., Lichtfuss, H.J., Fottner, L., 1987. Influence of free-stream turbulence and blade pressure gradient on boundary layer and loss behaviour of turbine cascades. ASME J. Turbomach. 109, 210–219.

Lardeau, S., Leschziner, M.A., 2006. Modeling of wake-induced transition in linear low-pressure turbine cascades. AIAA J. 44, 1854–1865.

Lardeau, S., Leschziner, M.A., Li, N., 2004. Modelling bypass transition with low-Reynolds-number nonlinear eddy viscosity closure. Flow Turbul. Combust. 73, 49–76.

Lardeau, S., Li, N., Leschziner, M.A., 2007. Large eddy simulation of transitional boundary layers at high free-stream turbulence intensity and implications for RANS modeling. ASME J. Turbomach. 129, 311–317.

Lodefier, K., Dick, E., 2005. Modelling of unsteady transition in low-pressure turbine blade flows with two dynamic intermittency equations. Flow Turbul. Combust. 76, 103–132.

Malkiel, E., Mayle, R.E., 1996. Transition in a separation bubble. ASME J. Turbomach. 118, 752–759.

Mayle, R.E., 1991. The role of laminar-turbulent transition in gas turbine engines. ASME J. Turbomach. 113, 509–537.

Mayle, R.E., Schulz, A., 1997. The path to predicting bypass transition. ASME J. Turbomach. 119, 405–411.

Menter, F.R., Rumsey, C.L., 1994. Assessment of two-equation turbulence models for transonic flows. AIAA Paper 94-2343.

Merkle, C.L., 1995. Preconditioning methods for viscous flow calculations. In: Hafez, M., Oshima, K. (Eds.), Computational Fluid Dynamics. John Wiley & Sons, pp. 419–436.

Michelassi, V., Martelli, F., Dénos, R., Arts, T., Sieverding, C.H., 1999. Unsteady heat transfer in stator–rotor interaction by two-equation turbulence model. ASME J. Turbomach. 121, 436–447.

Papanicolaou, E.L., Rodi, W., 1999. Computation of separated-flow transition using a two-layer model of turbulence. ASME J. Turbomach. 121, 78–87.

Praisner, T.J., Clark, J.P., 2007. Predicting transition in turbomachinery – Part I: A review and new model development. ASME J. Turbomach. 129, 1–13.

Pulliam, T.H., Chaussee, D.S., 1981. A diagonal form of an implicit factorization algorithm. J. Comput. Phys. 39, 347–363.

Savill, A.M., 1993a. Further progress in the turbulence modeling of by-pass transition. In: Rodi, W., Martelli, F. (Eds.), Engineering Turbulence Modeling and Experiments, vol. 2. Elsevier Science, pp. 583–592.

Savill, A.M., 1993b. Some recent progress in the turbulence modeling of by-pass transition. In: So, R.M.C., Speziale, C.G., Launder, B.E. (Eds.), Near-Wall Turbulent Flows. Elsevier Science, pp. 829–848.

Savill, A.M., 2002. By-pass transition using conventional closures. In: Launder, B., Sandham, N. (Eds.), Closure strategies for turbulent and transitional flows. Cambridge University Press, pp. 464–492.

Schlichting, H., 1968. Boundary-Layer Theory, sixth ed. McGraw Hill Co.

Steelant, J., Dick, E., 1996. Modeling of bypass transition with conditioned Navier–Stokes equations coupled to an intermittency transport equation. Int. J. Numer. Meth. Fluids 23, 193–220.

Steger, J.L., Warming, R.F., 1981. Flux vector splitting of the inviscid gas-dynamic equations with applications to finite difference methods. J. Comput. Phys. 40, 263–293.

Suzen, Y.B., Huang, P.G., 2000. Modeling of flow transition using an intermittency transport equation. ASME J. Fluids Eng. 122, 273–284.

Suzen, Y.B., Huang, P.G., 2005. Numerical simulation of unsteady wake/blade interactions in low-pressure turbine flows using an intermittency transport equation. ASME J. Turbomach. 127, 431–444.

Suzen, Y.B., Xiong, G., Huang, P.G., 2002. Predictions of transitional flows in low-pressure turbines using an intermittency transport equations. AIAA J. 40 (2), 254–266.

Venkateswaran, S., Weiss, S., Merkle, C.L., Choi, Y.H., 1992. Propulsion related flow fields using the preconditioned Navier–Stokes equations. AIAA Paper 92-3437.

Vicedo, J., Vilmin, S., Dawes, W.N., Savill, A.M., 2004. Intermittency transport modeling of separated flow transition. ASME J. Turbomach. 126, 424–431.

Volino, R.J., 1998. A new model for free-stream turbulence effects on boundary layers. ASME J. Turbomach. 120, 613–620.

Volino, R.J., 2005. An investigation of the scales in transitional boundary layers under high free-stream turbulence conditions. Exp. Fluids 38, 516–533.

Walters, D.K., Leylek, J.H., 2004. A new model for boundary-layer transition using a single-point RANS approach. ASME J. Turbomach. 126, 193–202.

Walters, D.K., Leylek, J.H., 2005. Computational fluid dynamics study of wake-induced transition on a compressor-like flat plate. ASME J. Turbomach. 127, 52–63.

Westin, K.J.A., Henkes, R.A.W.M., 1997. Application of turbulence models to bypass transition. ASME J. Fluids Eng. 119, 859–866.

Wilcox, D.C., 1998. Turbulence Models for CFD. DCW Industries, Inc.